

Data imputation in in situ measured particle size distributions by means of neural networks

Pak Lun Fung^{1,2}, Martha Arbayani Zaidan^{1,2,3}, Ola Surakhi⁴, Sasu Tarkoma⁵, Tuukka Petäjä^{1,3} and Tareq Hussein^{1,6,7}

¹Institute for Atmospheric and Earth System Research / Physics, Faculty of Science, University of Helsinki, Finland; pak.fung@helsinki.fi; martha.zaidan@helsinki.fi; tuukka.petaja@helsinki.fi; tareq.hussein@helsinki.fi

²Helsinki Institute of Sustainability Science, Faculty of Science, University of Helsinki, Finland

³Joint International Research Laboratory of Atmospheric and Earth System Sciences, School of Atmospheric Sciences, Nanjing University, Nanjing 210023, China

⁴Department of Computer Science, The University of Jordan, Amman 11942, Jordan; ola.surakhi@gmail.com

⁵Department of Computer Science, Faculty of Science, University of Helsinki, Finland; sasu.tarkoma@helsinki.fi

⁶Department Material Analysis and Indoor Chemistry, Fraunhofer WKL, D-38108 Braunschweig, Germany

⁷Department of Physics, The University of Jordan, Amman 11942, Jordan

Correspondence to: Pak Lun Fung and Tareq Hussein

Abstract.

In air quality research, often only size-integrated particle mass concentrations as indicators of aerosol particles are considered. However, the mass concentrations do not provide sufficient information to convey the full story of fractionated size distribution, in which the particles of different diameters (D_p) are able to deposit differently on respiratory system and cause various harm. Aerosol size distribution measurements rely on a variety of techniques to classify the aerosol size and measure the size distribution. From the raw data the ambient size distribution is determined utilising a suite of inversion algorithms. However, the inversion problem is quite often ill-posed and challenging to solve. Due to the instrumental insufficiency and inversion limitations, imputation methods for fractionated particle size distribution are of great significance to fill the missing gaps or negative values. The study at hand involves a merged particle size distribution, from a scanning mobility particle sizer (NanoSMPS) and an optical particle sizer (OPS) covering the aerosol size distributions from 0.01 to 0.42 μm (electrical mobility equivalent size) and 0.3 μm to 10 μm (optical equivalent size) and meteorological parameters collected at an urban background region in Amman, Jordan in the period of 1 Aug 2016–31 July 2017. We develop and evaluate feed-forward neural network (FFNN) approaches to estimate number concentrations at particular size bin with (1) meteorological parameters, (2) number concentration at other size bins, and (3) both of the above as input variables. Two layers with 10–15 neurons are found to be the optimal option. Worse performance is observed at the lower edge ($0.01 < D_p < 0.02 \mu\text{m}$), the mid-range region ($0.15 < D_p < 0.5 \mu\text{m}$) and the upper edge ($6 < D_p < 10 \mu\text{m}$). For the edges at both ends, the number of neighbouring size bins is limited and the detection efficiency by the corresponding instruments is lower compared to the other size bins. A distinct performance drop over the overlapping mid-range region is due to the deficiency of a merging algorithm. Another plausible reason for the poorer performance for finer particles is that they are more effectively removed from the atmosphere compared to the coarser particles so that the relationships between the input variables and the small particles is more dynamic. An observable overestimation is also found in early morning for ultrafine particles followed by a distinct underestimation before midday. In the winter, due to a possible sensor drift and interference artefacts, the estimation performance is not as good as the other seasons. The FFNN approach by meteorological parameters using 5-min data ($R^2 = 0.22\text{--}0.58$) shows poorer results than data with longer time resolution ($R^2 = 0.66\text{--}0.77$). The FFNN approach by the number concentration at the other size bins can serve as an alternative way to replace negative numbers in size distribution raw dataset thanks to its high accuracy

42 and reliability ($R^2 = 0.97-1$). This negative numbers filling approach can maintain a symmetric distribution of errors and
43 complement the existing ill-posed built-in algorithm in particle sizer instruments.

44

45 **Keywords.**

46 ~~Atmospheric aerosols particles~~, ~~Aerosol size distribution~~, feed-forward neural network, ~~atmospheric aerosols~~
47 ~~particles~~ interpolation, missing data, SMPS, OPS

48 **1 Introduction**

49 Particulate matter (PM) is the principal component of air pollution. PM includes a range of particle sizes, such as coarse
50 ($1 < \text{particle diameter } (D_p) < 10 \mu\text{m}$), fine ($0.1 < D_p < 1 \mu\text{m}$), and ultrafine particles (UFP, $D_p < 0.1 \mu\text{m}$). Through human's
51 inhalation, coarse particles usually are partly deposited in the head airway ($5-30 \mu\text{m}$) by the inertial impaction mechanism,
52 and are partly deposited in the tracheobronchial region, mainly through sedimentation ($1-5 \mu\text{m}$). The particles may be
53 further absorbed or removed by mucociliary clearance (Gupta and Xie, 2018). The remaining fine and UFP, due to their
54 high surface area to mass ratios (Kreyling et al., 2004), penetrate deeply into the alveolar region, where removal
55 mechanisms may be insufficient (Gupta and Xie, 2018). Evidence suggests that the adverse associations of short-term
56 UFP exposure with acute and chronic problems ranging from inflammation, exacerbation of asthma, and metal fume fever
57 to fibrosis, chronic inflammatory lung diseases, and carcinogenesis (Spinazzè et al., 2017) might be at least partly
58 independent of other pollutants (Ohlwein et al., 2019). Various studies have demonstrated that inhaled or injected UFP
59 could enter systemic circulation and migrate to different organs and tissues (Londahl et al., 2014; Xing et al., 2016).

60

61 Other than health effects, particles of various sizes also contribute to Earth's ecosystem and climate differently. For
62 instance, fine and UFP are capable of growing up to diameters of $0.02-0.1 \mu\text{m}$ within a day (Kulmala et al., 2004;
63 Kerminen et al., 2018) where they constitute a fraction of cloud condensation nuclei; thus, indirectly affecting the climate
64 (Kerminen et al., 2012). The drivers behind aerosol particles vary between natural and anthropogenic as well as primary
65 and secondary. Primary particles are emitted to the atmosphere as particles, such as sea salt or dust particles, while
66 secondary particles form in the atmosphere through gas-to-particle transformation, which has been known as new particle
67 formation (NPF) observed in various environments and contributing to a major fraction of the total particle number budget
68 (Kulmala et al., 2004; Kerminen et al., 2018). In addition, while fine particles cool the climate by predominantly scattering
69 shortwave radiation, coarse particles warm the climate system by absorbing both shortwave and longwave radiation (Kok
70 et al., 2017). Indeed, the complexity of urban aerosols is tribute to the fact that several sources can contribute in the same
71 particle size range (Rönkkö et al., 2017).

72

73 Currently, the most commonly reported aerosol variables are particle mass concentration and particle number
74 concentration. The former metric, which is dominated by coarser particles, is included as air quality indicators (e.g. mass
75 concentrations of both thoracic particles PM_{10} and fine particles $\text{PM}_{2.5}$); however, it has been argued that this might ignore
76 the potential adverse effect of UFP on health (Zhou et al., 2020). The latter one describes better the distribution of finer
77 particles, but it neglects the influence of coarse particles. Using either particle mass concentration or particle number
78 concentration solely is not enough to fully review the health effects and the Earth's climate system by aerosol particles.
79 Therefore, in order to understand the origin of atmospheric aerosol particles and their potential impacts at a specific
80 location, the whole size distribution of these particles needs to be studied (Zhou et al., 2020).

81
82 Recently, due to urbanization and increased population, megacities have increased their contribution to atmospheric
83 aerosol pollution massively Lelieveld et al. (2015). Middle East and North Africa (MENA) regions, with an average
84 annual growth rate of 1.74% in 2019 (World Bank Group, 2019), has one of the world's regions most rapidly expanding
85 populations. With the population of 578 million, several cities in MENA regions are among the 20 most polluted cities in
86 the world. The annual average concentrations of some pollutants, for example PM_{2.5} in MENA (54.0 µg m⁻³) often exceed
87 5 times the WHO recommended levels (10.0 µg m⁻³) (World Health Organisation, 2019). Many countries in MENA are
88 dealing with negative impacts of air pollution in terms of both economic burden and health aspect (Ahmed et al., 2017;
89 Goudarzi et al., 2019). Air Pollution in this region is estimated to cause 133,000 premature deaths annually, almost half
90 of which are attributed to natural sources of air pollution, such as windblown sea salt and desert dust (Gherboudj et al.,
91 2017). Apart from natural pollutants, anthropogenic activities also play a major role in driving the air quality. They include
92 the extensive development of petrochemical industry, vehicular emissions and open burning of waste (Arhami et al.,
93 2018).

94
95 However, aerosol studies in this region have not paid attention to the aerosol number size distribution so far. Among the
96 few studies published, most report mass concentration (Goudarzi et al., 2019; Arhami et al., 2018; Borgie et al., 2016),
97 while some focused on the total particle number in MENA regions. Studies on the size-fractionated number concentrations
98 are, nonetheless, scarce (e.g. Hakala et al., 2019) due to the unavailability of instruments for measuring UFP in many
99 air quality monitoring stations (Spinazzè et al., 2017). Determining aerosol number size distribution for a wide size range
100 in a reliable manner is a challenging task. The fact that the ambient distributions range from nanometers to several
101 micrometers dictates the use of multiple sizing techniques. For the sub-micron size range, electrical mobility equivalent
102 diameter is commonly used as the size parameter and the measurements are performed with Differential Mobility Particle
103 Sizer (DMPS) or Scanning Mobility Particle Sizer (SMPS) instruments (e.g. Wiedensohler et al., 2012). These systems
104 determine the aerosol size according to electrical mobility equivalent size. The larger particles (approximately > 0.3 µm)
105 can be classified according to their aerodynamic or optical size (Kulkarni et al., 2011). In order to obtain the full aerosol
106 size distribution, this data needs to be merged. Unfortunately this task is not trivial as the merging requires knowledge on
107 the chemical composition (influencing the refractive index and thus the optical size), shape (influencing electrical mobility
108 equivalent size), or effective density (influencing aerodynamic size) (Kannosto et al., 2008).

109 In addition, the raw data from these instruments must be inverted to obtain the particle size distribution. This is not a
110 straightforward problem. A proper inversion algorithm is required to restore the particle size distribution from the raw
111 response (Cai et al., 2018) using recorded kernel functions which describe the probability of particles of a certain size
112 being measured at a certain flow rate, influenced by the measured activation curves and the detection efficiencies of the
113 instruments (Lehtipalo et al., 2014). Depending on the instruments used and the measurement environments, some use a
114 built-in inversion algorithm in the instruments, which replace negative raw values with artificial non-negative numbers.
115 Some develop their own inversion methods; however, they all have their drawbacks. Examples include that the least
116 square method may magnify the random errors in the raw counts in Condensation Particle Counter (CPC) into relatively
117 large uncertainties (Enting and Newsam, 1990), the stepwise method may cause non-negligible errors (Lehtipalo et al.,
118 2014), and that the smoothing step method may introduce bias in the shape of the inverted distribution function
119 (Markowski, 1987). Kandlikar and Ramachandran (1999) pointed out that there is not a single universal inversion
120 algorithm applicable to all situations. In this study, the built-in inversion algorithm was used. This algorithm can lead to

121 negative values when the kernel functions are not optimally configured, especially in the size range of low number
122 concentration. These negative values have no physical meanings. Some experts in the in situ measurement community
123 might just omit the negative values or simply use nearest neighbour linear interpolation to replace the negative values.
124 However, the former method might cause asymmetric error for very small measured number concentration values (Viskari
125 et al., 2012), while the latter could result in too high values concurrently. To fill this knowledge gap, statistical estimation
126 methods can serve as an alternative to estimate of size-fractioned number concentration by using other available
127 measurements.

128
129 The main objective of the paper is to estimate particle number concentration/ fill the negative values making up for the
130 shortcomings of the built-in inversion algorithm in particle sizer instruments. Extending from the previous study by
131 Zaidan et al. (2020), we build our imputation method with a finer temporal and size-bin resolution. In order to do so, we
132 place emphasis on estimating particle number concentration of a specific size bin by the interaction with other size bins
133 and meteorological variables. In this study, we propose three approaches in terms of different input variables by means
134 of neural networks: (1) only meteorological parameters, (2) only particle size distribution, and (3) both particle size
135 distribution and meteorological parameters. Based on the general data analysis of the particle size distribution and the
136 meteorological condition, we explain the source of different size bins at certain weather conditions and the correlation
137 among the particle size distribution and meteorological parameters in Sect. 3. We evaluate the proposed neural network
138 method and compare it with other simpler methods in Sect. 4.1. In Sect. 4.2, we further discuss the temporal pattern of
139 the proposed method in terms of its diurnal cycle, weekend effect and seasonal variation. Besides, we examine the possible
140 technical reasons for the pattern found and the application of the proposed method.

141 **2 Methods**

142 **2.1 Measurement sites and Instruments**

143 In this study, we collected a dataset obtained from a measurement campaign in Amman, the capital city of Jordan, between
144 1 August 2016 and 31 July 2017. The city represents an area with Middle Eastern urban conditions within the Middle
145 East and North Africa (MENA) region. This region serves as a compilation of different aerosol particle sources including
146 natural dust, anthropogenic pollution (e.g. generated from the petrochemical industry and urbanization), as well as new
147 particle formation.

148
149 The database includes particle size distribution and meteorological parameters, as mentioned in the first step in [Figure 1](#) ~~Figure-1~~.
150 The aerosol measurement was carried out at the aerosol laboratory located on the third floor of the Department of Physics,
151 University of Jordan (32°00' N, 35°52' E) in the neighbourhood of Al Jubeiha. The campus is situated at an urban
152 background region in northern Amman. In particular, the campaign measured the particle number size distribution using
153 a scanning mobility particle sizer (NanoScan SMPS 3910, TSI, MN, USA) with default settings. It monitors the particle
154 size distributions as electrical equivalent diameter 0.01–0.42 μm (13 channels). The size range of the SMPS system can
155 be extended to coarse particles with an additional compact instrument: an optical particle sizer (OPS 3330, TSI, MN,
156 USA). OPS measures optical diameter 0.3–10 μm (13 channels). This optical sizing method reports an optical particle
157 diameter, which is often different from the electrical mobility diameter measured by the SMPS technique. The
158 measurements were combined to provide a particle size distribution of wider particle diameter range 0.01–10 μm , which

159 is further described in Sect. 2.2. The SMPS inlet consists of copper tubing with a diffusion drier (TSI 3062-NC). The inlet
160 flow rate was 0.75 lpm ($\pm 20\%$) while the sample flow rate was 0.25 lpm ($\pm 10\%$). The flow rate of OPS was about 1 lpm.
161 The aerosol transport efficiency and losses through the aerosol inlet assembly and the diffusion drier was determined
162 experimentally in the laboratory: ambient aerosol sampling alternatively with and without sampling inlet, and the aerosol
163 data was corrected accordingly. The penetration efficiency was $\sim 47\%$ for $0.01\ \mu\text{m}$, $\sim 93\%$ for $0.3\ \mu\text{m}$ and $\sim 40\%$ for 10
164 μm (Hussein et al., 2020). These deficiency of measurement at the upper and lower edges is somewhat in alignment with
165 other literatures. Particle size measured by nanoSMPS (Tritscher et al., 2013) tended to be underestimated for spherical
166 particles larger than $0.2\ \mu\text{m}$ by up to 34% (Fonseca et al., 2016). Liu et al. (2014) clearly portrayed that the detection limit
167 of particle size below $0.03\ \mu\text{m}$ is about $80\text{--}500\ \text{cm}^{-3}$, which is up to 10 times larger than that of coarser particles, for other
168 versions of SMPS. Stolzenburg and McMurry (2018) explained that discrepancies could be resulted from Differential
169 Mobility Analysers (DMAs) with transfer functions that were degraded (i.e., broadened) by flow distortions caused by
170 particle deposition within the classifier tube, sizing errors due to errors in flowmeter calibrations or leaks, CPC
171 concentration errors due to improper pulse counting, and continuity failure in the DMA high voltage connection.

172

173 The meteorological measurement was performed with a weather station (WH-1080, Clas Ohlson: Art.no.36-3242,
174 Helsinki, Finland) with a time resolution of 5 minutes. The meteorological data were comprised of ambient temperature
175 (Temp, resolution $0.1\ ^\circ\text{C}$), relative humidity (RH, resolution 1%), wind speed (WS), wind direction (WD, 16 equal
176 divisions) and air pressure (P, resolution $0.3\ \text{hPa}$) (Hussein et al., 2019; Hussein et al., 2020; Zaidan et al., 2020). Wind
177 direction is resolved into north and east direction, as WD-N and WD-E, respectively. The data collection process is
178 illustrated in the first step in the database block in [Figure 1](#).

179 2.2 Data pre-processing

180 The next step in the database block in [Figure 1](#) is data pre-processing. Since the sampling time resolution of SMPS and
181 OPS was 1 min and 5 min, respectively, we synchronised the data into 5-min averages. Since a part of the size ranges in
182 both instruments are overlapping with each other, the last two size bins in SMPS and the first size bin in OPS were
183 neglected. Finally, we merged the size range of electrical mobility diameter $0.01\text{--}0.25\ \mu\text{m}$ by SMPS and optical diameter
184 $0.32\text{--}10\ \mu\text{m}$ by OPS, and obtain a wider particle size distribution which covers the diameter range $0.01\text{--}10\ \mu\text{m}$. Merging
185 electrical mobility diameter and optical diameter can be a challenge and the overlapping region is often calculated with
186 high uncertainty (DeCarlo et al., 2004; Tritscher et al., 2015). The challenge arises because the optical diameters are
187 measured based on the refractive index of the particles, which depends on their chemical composition. Therefore, the
188 sizing will vary over time. There is also a slight dependency with the SMPS system that is linked to the shape of the
189 particles, which influences their sizing.

190

191 We also calculated the particle number concentration with four particle diameter modes (size-fractionated number
192 concentration): nucleation ($0.01\text{--}0.025\ \mu\text{m}$), Aitken ($0.025\text{--}0.1\ \mu\text{m}$), accumulation ($0.1\text{--}1\ \mu\text{m}$) and coarse mode ($1\text{--}10$
193 μm). Subsequently, the total number concentration was obtained as the sum of all these fractions. The size-fractionated
194 number concentrations were obtained by summing up the measured particle number size distribution over the specified
195 particle diameter range.

196

197 In order to perform data imputation with neural networks, aerosol and meteorological data were first linearly interpolated
 198 in time in case of short missing data periods. For missing data over longer periods, the whole rows are eliminated. The
 199 shorter missing data occurs due to technical faults while the longer missing periods are attributed to instrument
 200 maintenance (Zaidan et al., 2020). Only 71.8% of total data was retained for the next step in the measurement period.
 201 Since the data were obtained from different measured variables with various physical units and magnitudes, it was crucial
 202 to normalise the data. The scaling factor depends on which activation function is chosen. In this case, the datasets were
 203 scaled so that it has a mean of 0 and a standard deviation of 1 to transform them into the range of the activation function.
 204 The standardised data was then separated into different months for the reason of the seasonal variation in the atmospheric
 205 condition. The data was further divided into training set (70%) and testing set (30%). The processed data were also
 206 converted to hourly and daily averages for reporting purposes.

207 2.3 Setting of the neural network

208 After data collection and data pre-processing procedures, the next step is method optimisation (Figure 1). ANN models
 209 have been utilised in predicting air quality (Freeman et al., 2018; Maleki et al., 2019; Cabaneros et al., 2019; Zaidan et
 210 al., 2020; Fung et al., 2020). Neural networks provide a robust approach for approximating real-valued target functions
 211 because they can mimic the non-linearity of the functions and their optimisation methods are well developed (Zaidan et
 212 al., 2017). The architecture of neural networks consists of nodes as activation function (Figure 2), and the activation
 213 function in each layer determines the output value of each neuron that becomes the input values for neurons in the next
 214 hidden layer connected to it. In this paper, feed-forward neural network (FFNN) is used instead of a more sophisticated
 215 time delay neural network (TDNN) because some of the rows in the dataset were removed in the data pre-processing step
 216 due to the existence of missing data and TDNN cannot be performed without time continuity. FFNN usually consists of
 217 a series of layers. The first layer has a connection from the network input. Each subsequent layer has a connection from
 218 the previous layer. The final layer produces the network's output. A neuron can be thought as a combination of two parts:

$$z_j^{(L)} = \sigma\left(\sum_{i=1}^n w_{ji}^{(L)} x_i + b_j^{(L)}\right) \quad (1),$$

219 where $z_j^{(L)}$ and $b_j^{(L)}$ are the intermediate output and the bias term for the j^{th} neuron at L^{th} layer, respectively. $w_{ji}^{(L)}$ is the j^{th}
 220 weight for each data points x_i at L^{th} layer. The second part performs the activation function (sigmoid function in this
 221 study) on z_j to give out the output of the neuron:

$$\sigma(z_j^{(L)}) = \frac{1}{1 + \exp^{-z_j^{(L)}}} \quad (2),$$

222 The FFNN method was created, trained and simulated with MATLAB (version: 8.3.0.532), using Neural Network
 223 Toolbox. We initialised the weights randomly and the weights were updated through ‘‘Levenberg-Marquardt’’ algorithm
 224 optimisation that was the fastest available back-propagation training function (Chaloulakou et al., 2003). We performed
 225 several iterations within a cycle to minimise the training loss with Bayesian regularisation. These steps were done
 226 iteratively until the best combination of the number of hidden layers and the corresponding number of neurons that
 227 provided the minimum error was found. According to the review paper by Cabaneros et al. (2019), a shallow neural
 228 network with one hidden layer and enough neurons in the hidden layers can fit any finite input-output mapping problem
 229 for non-linear relationship. In the network training process, the number of neurons varied from 2 to 10 neurons per layer
 230 with an incremental factor of 2 neurons in each simulation, and from 10 to 25 per layer with an incremental factor of 5
 231 neurons in each simulation. To keep the method simple, we consider only one or two layers in the simulation process

232 because the computing requirements could rise exponentially with the number of layers and neurons. Once we pick the
233 suitable method configuration, the method estimates number concentration using testing data. Finally, the selected
234 performance metrics, described in Section 2.4, can be calculated and we evaluate which approach is the most suitable for
235 size distribution estimation.

236 2.4 Other methods as comparison with the neural network method

237 In order to demonstrate the performance of the FFNN method, we perform similar procedures applying other simpler
238 methods, which have been widely used as means of data imputation (Junger and Ponce De Leon, 2015). They include
239 univariate and multivariate methods. The former includes unconditional mean (UM), median (MD), linear interpolation
240 (LinI), logarithmic interpolation (LogI), next neighbour interpolation (nNI) and previous neighbour interpolation (pNI),
241 where nNI was implemented as the next value carried backward while pNI as the previous value carried forward. The
242 multivariate methods used in this study are conditional mean based on a linear regression of meteorological parameters
243 and other particle size number concentrations as inputs (CM–met and CM–PSD, respectively). These methods are
244 implemented as a comparison with the FFNN method.

245 2.5 Performance metrics

246 We choose the optimal combination of the number of hidden layers and the corresponding number of neurons by checking
247 its mean absolute error (MAE), which is a simple way to illustrate the residuals of the estimated values by the estimation
248 method. In order to identify which size bin manage to be predicted best, two metrics are used, namely coefficient of
249 determination (R^2) and normalised root-mean-square error (NRMSE). R^2 measures how well the observed outcomes are
250 replicated by the estimation method, based on the proportion of total variation of outcomes explained by the estimation
251 method. NRMSE represents the standard deviation of the estimated errors with respect to its mean. NRMSE is used rather
252 than commonly used RMSE because the number concentrations of the different size range are of different magnitudes.
253 The comparison in different size range becomes different if RMSE is not normalised with its mean.

$$\text{MAE} = \frac{\sum_{i=1}^n |y_i - \hat{y}_i|}{n} \quad (3)$$

$$R^2 = 1 - \frac{\sum_{i=1}^n (y_i - \hat{y}_i)^2}{\sum_{i=1}^n (y_i - \bar{y})^2} \quad (4)$$

$$\text{NRMSE} = \frac{\sqrt{\frac{\sum_{i=1}^n (y_i - \hat{y}_i)^2}{n}}}{\bar{y}} \quad (5)$$

254 where y_i , \hat{y}_i and \bar{y} represent the i^{th} measurement value, the y^{th} estimated value by the estimation method and the mean of
255 the all the measurement data, respectively. n notates the total number of the valid measurement data.

256 3 General data analysis

257 3.1 Environmental condition

258 Hussein et al. (2019) and Zaidan et al. (2020) investigated and described the effect of local weather conditions,
259 respectively. Here we describe briefly the meteorological conditions during the measurement period as background
260 information. Starting from August 2016, the daily temperature decreased gradually from 40°C to its tough 0°C in February
261 2017. It rose gradually to 40°C in August 2017. During the measurement period, the hourly median value was 19.9°C

Formatted: Finnish

Field Code Changed

Formatted: Finnish

Field Code Changed

Formatted: Finnish

262 (Figure 3a). RH varied quite a lot from 10% to 100%, with an hourly median of 52.3%, and did not seem to have a
263 seasonal pattern (Figure 3b). In summer months, wind appeared to be stronger but the wind direction is more stable, mostly
264 from northwest (270°–360°). In cold months, averaged wind speed was lower but wind blew from fluctuating direction.
265 During the whole measurement period, wind speed ranged between 0–6 m s⁻¹ and its median is 1.39 m s⁻¹ (Figure 3c–d).
266 Air pressure varied in a range from 892 to 912 hPa and its hourly median was 900 hPa. In spite of the narrow range of
267 variation, winter months seem to have slightly higher air pressure than summer months (Figure 3e).

268
269 Meteorological conditions have been suggested to influence particle number concentration. Hussein et al. (2019)
270 demonstrated that number concentration had a rather complex relationship with temperature. Furthermore, number
271 concentration of submicron had a decreasing trend with respect to the wind speed which indicates that most of the
272 submicron fraction is originated from local sources such as combustion processes. Meanwhile, the number concentration
273 of coarse particles had higher concentrations at stagnant conditions and when the wind speed is higher than 5.5 m s⁻¹. It
274 is mainly because of road dust resuspension and might also be attributed to dust storm via long-range transport Hussein
275 et al., 2019. In this study, we further explore how wind direction influences the particle number concentration (Figure 4).
276 Wind coming from the northwest (225°–325°) was generally stronger, but lower particle number concentration was
277 detected because the measurement area is at the outskirts of downtown. Wind from East and South (45°–225°) has a lower
278 wind speed but a more intense hourly particle number concentration can be detected. From that direction sits the
279 urban city where all kinds of industrial activities take place. When considering only coarse particles, relatively high
280 number concentration is found when south-westerly wind is strong. This can further serve as an evidence that the source
281 of coarse particles in that region might come mostly from long range sea salt from Dead Sea or dust particles from nearby
282 deserts.

283 3.2 General pattern of particle size distribution

284 Hourly total number concentration ranged from $1.90 \times 10^3 \text{ cm}^{-3}$ to $1.52 \times 10^5 \text{ cm}^{-3}$ and its median was $1.36 \times 10^4 \text{ cm}^{-3}$. Figure
285 5a performed moderate seasonal pattern in general: lower in summer months and higher in colder months. Hussein et al.
286 (2019) also characterised the modal structure of the particle number size distribution for the same site. Four modes have
287 been detected by lognormal fitting, as known as DO-FIT algorithm and modal structure (Hussein et al., 2005; Hussein et
288 al., 2019), revealed that the mode number concentrations of the nucleation, Aitken, and coarse modes were lognormally
289 distributed around their geometric mean values: 0.022 μm, 0.062 μm, and 2.3 μm respectively. However, the accumulation
290 mode number concentration had two distinguished modes with particle diameter centred at 0.017 μm and 0.39 μm. As
291 seen in Table 1, the total number concentration of all particle size ($1.70 \pm 1.26 \times 10^4 \text{ cm}^{-3}$) is mostly accounted by Aitken
292 mode (45–80%, average: $1.09 \pm 1.01 \times 10^4 \text{ cm}^{-3}$), followed by nucleation mode (10–50%, average: $0.48 \pm 0.32 \times 10^4 \text{ cm}^{-3}$).
293 Accumulation mode (0–15%, average: $0.13 \pm 0.08 \text{ cm}^{-3}$) comes third and only less than 0.5% of the total particle number
294 concentration contain coarse particles with an average of $2.13 \pm 2.80 \text{ cm}^{-3}$ (Figure 5b–e). Seasonal pattern of the total
295 number concentration resembles the Aitken composition: lower proportion in summer months and higher in colder
296 months. The ratio of nucleation mode performs in an opposite way. The seasonal variation of total number concentration
297 is due to the more suppressed boundary layer in winter (Teinilä et al., 2019) and the elevated wood combustion (Hellén
298 et al., 2017). The particle number of accumulation and coarse mode steadily stay at a low proportion line, which did not
299 account for the total number concentration. It is also noticed that dust episodes occurred with the concentrations that often

300 exceeded 2 cm^{-3} and the daily concentration in the course of these episodes can rise to 20 cm^{-3} . These episodes were often
301 found in spring from February to May and some episodes can last for up to one week.

302
303 Similar to many other urban environments, the diurnal pattern observed in this study reflects the combustion emissions
304 from traffic activity, which is more during the workdays (Hussein et al., 2019). The two peaks of the nucleation mode
305 and Aitken mode in the cold months are relevant for the morning and the afternoon traffic rush hours, which are similar
306 to those noticed in most cities in other countries. In warmer months, the diurnal cycles are not as distinct, but a sharp peak
307 of nucleation mode around noon is found, which is associated with the occurrence of new particle formation. These events
308 occurred very often in the summer as suggested by Hussein et al. (2020). The amplitude of diurnal cycles of coarse mode
309 is small while the patterns of accumulation are not clear (Figure 6Figure-6).

310 3.3 Correlation analysis

311 Figure 7Figure-7 demonstrated the interaction among the whole measured spectrum shows three range clusters based on their
312 correlation with the number concentration at other bin sizes: $0.01\text{--}0.205 \mu\text{m}$, $0.205\text{--}0.875 \mu\text{m}$ and $0.875\text{--}10 \mu\text{m}$. 0.01--
313 $0.205 \mu\text{m}$ and $0.875\text{--}10 \mu\text{m}$ fall entirely within the size range detected by SMPS and OPS, respectively. The 5-min number
314 concentration of smaller size and bigger size bins have clear and strong correlation with the concentration of its
315 neighbouring size bin. However, particles of size $0.205\text{--}0.875 \mu\text{m}$ are located in the overlapping regions by the two
316 instruments; as a result, do not correlate well with other size bins. The correlation of 5-min particle size distribution with
317 meteorological parameters are generally low. Temperature appears to be the most correlated parameters for all bin sizes
318 among all the parameters we used in this study. Smaller size range have higher Pearson's correlation coefficient (R) than
319 larger size range for WD, WS and P.

320
321 The 5-min averaged data show similar correlation for the particle size distribution except for the smallest size bin. The
322 hourly and daily data have higher correlation with the other size bins which are also monitored by SMPS. The 5-min
323 averaged data show different correlation from the hourly and daily averaged data performed by Zaidan et al. (2020). The
324 correlations of 5-min size distribution with all meteorological variables are below 0.5 for all size range. However, for
325 hourly and daily averaged data, R is much higher in specific size bins. Hourly and daily temperature, in particular, show
326 increasing R with larger particle size for accumulation and coarse mode. Overall, the correlations increase with the longer
327 averaging windows. This might be due to the buffer period the meteorological conditions act on the dispersion of particles.
328 Based on this result, using data with finer temporal resolution might be considered to be less influential to the estimation
329 accuracy.

330 4 Evaluation of the proposed method

331 4.1 General evaluation

332 Figure 8Figure-8 illustrates how well the three approaches of the proposed FFNN perform in term of R^2 and NRMSE.
333 Approach 1 (Size distribution estimation based on meteorological parameters only, FFNN-met): For more than half
334 out of the 23 size bins, 2 layers and 15 neurons is the best combination where the residuals are the lowest (Table 2Table-2).
335 Owing to the poor correlation with meteorological condition, we expect a low correlation of determination even using the
336 optimal configuration neural network ($R^2 = 0.22\text{--}0.58$). The R^2 are low at the nucleation mode ($0.01 < D_p < 0.03 \mu\text{m}$) of

337 the whole size distribution around nucleation mode ($R^2 \sim 0.2$). The rest of the size bins have better and more stable
338 performance ($R^2 = 0.4\text{--}0.58$). This shows that the instrument might have a poor detection efficiency for particles of smaller
339 size. The performance of FFNN method using 5-min data for all size bins ($R^2 = 0.22\text{--}0.58$) is worse than using daily data
340 ($R^2 = 0.77$) performed in Zaidan et al. (2020). Compared with hourly data ($R^2 = 0.66$), the overall performance of the
341 method using 5-min data is comparable ($R^2 = 0.67$).

342 **Approach 2 (Size distribution estimation based on other particle sections only, FFNN-PSD):** This approach works
343 well with most combination of number of layers and neurons. They do not show a clear difference among the combinations
344 we choose. There is no single combination which entirely outperform the others in all size bins. We summed up the MAE
345 for all size bins and decided to stick to 2 layers and 10 neurons with the overall lowest residuals (Table 2-Table 2). R^2 are all
346 above 0.97 for all bin sizes, and NRMSE are 0.01–0.25 for all bin sizes. The results are expected because there are 22
347 inputs and one output. Relatively worse correlation at the edges of size bins ($0.01 < D_p < 0.02 \mu\text{m}$; $6 < D_p < 10 \mu\text{m}$) is found
348 because of the lack of nearby size bins which has high correlation with the corresponding size bin. Another reason could
349 be that the instrument has a higher detection limits for smaller particles (Liu et al., 2014). The poorer performance for
350 smaller size might be due to a coarser sizer resolution compared to other SMPS components (Tritscher et al., 2013), so
351 that NanoSMPS does not reflect the real enough size distribution in the atmosphere. Relatively poor estimation
352 performance at the middle size range ($0.15 < D_p < 0.5 \mu\text{m}$) in the whole measured spectrum is because of the overlapping
353 of instruments. This also ascertain the importance of creating a better algorithm when we merge two or more size
354 distribution by different instruments. In this study, the measuring techniques and the measuring targets are different by
355 the SMPS and OPS. The merging of the two measuring targets, the optical particle diameter and the electrical mobility
356 diameter, might create significant uncertainties (DeCarlo et al., 2004; Tritscher et al., 2015). The estimation of certain bin
357 size by other bin sizes can be thought of replacing negative values in the raw data by particle sizers. While some instrument
358 manufacturers create built-in algorithms to replace with artificial non-negative numbers, most end-users simply remove
359 the seemingly impossible negative values from the dataset. The perfect way to do it is to have a parallel instrument that
360 overlaps with that particle size range. However, in many cases, this is not possible as a result of financial constraints.
361 Therefore, we shall rely on the mutual relationship between the size sections in the aerosol population. Negative values
362 appear often at size bins with very low number concentration (usually in coarse mode). Instead of eliminating them, this
363 alternative could maintain the symmetry of the error distribution of the number concentration (Viskari et al., 2012) and
364 minimise the uncertainties caused.

365 **Approach 3 (Size distribution estimation based on meteorological parameters and other particle sections):** The
366 general results are similar as in PSD. However, the more input variables do not enable the approach to work better. At
367 some bin size the R^2 are even slightly smaller than PSD solely. Since meteorological data show low correlation with most
368 portion of measured spectrum. In that approach, the addition of meteorological parameters is not beneficial to the
369 estimation process. Due to the lack of improvement in the method development, we will only focus on the two methods:
370 FFNN-met and FFNN-PSD from now on.

371
372 In order to highlight the performance of the FFNN methods in terms of accuracy and reliability, we compare the FFNN
373 methods with other simpler methods, the results as shown in Table 3-Table 3 for R^2 and Table 4-Table 4 for NRMSE. The R^2 of the
374 univariate methods UM and MD are close to 0 because their imputation are over-simplified and imply the replacement of
375 a missing value by a constant. [This can be further validated by the narrow range of the estimated particle concentrations](#)
376 [in Figure 9a–b](#). The remaining univariate interpolation methods LinI, LogI, nNI and pNI showed good results in general

377 ($R^2 = 0.82\text{--}0.92$, $\text{NRMSE} = 0.57\text{--}0.88$), but failed to perform even fairly at some particle size bins. This implies that these
378 methods are not stable for the whole spectrum of the particle size distribution. Some of the estimated particle
379 concentrations are off from the 1:1 line, which implies that the estimation of some particle bins are not as accurate (Figure
380 9c-f). The performance results of the multivariate methods CM-met and CM-PSD are comparable to FFNN-met and
381 FFNN-PSD, but both CM methods show weaker performance than FFNN methods in terms of R^2 and NRMSE no matter
382 whether meteorological (CM-met: $R^2 = 0.52$, $\text{NRMSE} = 1.39$; FFNN-met: $R^2 = 0.67$, $\text{NRMSE} = 1.13$) or particle size
383 distribution data (CM-PSD: $R^2 = 0.99$, $\text{NRMSE} = 0.17$; FFNN-PSD: $R^2 = 1.00$, $\text{NRMSE} = 0.07$) is used as inputs. The
384 pattern of performance of the multivariate methods is also similar to those of FFNN, i.e., relatively poor performance at
385 the edges of size bins ($0.01 < D_p < 0.02 \mu\text{m}$; $6 < D_p < 10 \mu\text{m}$) and the overlapping region ($0.15 < D_p < 0.5 \mu\text{m}$). When
386 combining the whole spectrum, FFNN methods (Figure 9i-j) appear to have narrower bands than CM methods (Figure
387 9g-h) along 1:1 line, which indicate the methods work similarly across the particle size spectrum. Although the
388 multivariate method CM-PSD (Figure 9h) also rely on the mutual relationship between the size sections in the aerosol
389 population, this method is not as accurate and stable as our proposed FFNN-PSD.

390
391 From the perspective of physics, particles in the nucleation mode ($0.01 < D_p < 0.03 \mu\text{m}$) are more sensitive to
392 transformation processes due to their volatility and rather unstable nature (Morawska et al., 2008). This leads to a
393 relatively short lifetime in the atmosphere (Al-Dabbous et al., 2017), hence, the relationships between the input variables
394 and the nucleation mode are not well established. Al-Dabbous et al. (2017) demonstrated that accumulation mode particles
395 ($0.1 < D_p < 0.3 \mu\text{m}$) have much longer lifetimes compared to smaller particles, causing them to be transported for larger
396 distances (Laakso et al., 2003); therefore, the mapping of the relationships between long-range transported accumulation
397 mode particles and covariates is supposed not to well understood. However, the relative prediction ability in this study is
398 not lower given that local meteorological variables were used as input variables. The possible reason is that this mode
399 falls exactly in the instrumental overlapping regions, which leads to a lower predictability. The locally-produced Aitken
400 mode particles ($0.033 < D_p < 0.1 \mu\text{m}$) are less effectively removed by transformation processes (e.g. evaporation and
401 coagulation) from the atmosphere, compared with nucleation mode ($0.01 < D_p < 0.033 \mu\text{m}$), allowing the estimation methods
402 to better understand their relationships with the input variables, which is in alignment with Al-Dabbous et al. (2017).

403 4.2 Temporal pattern

404 Figure 10Figure-9 shows the diurnal discrepancies during workdays and weekends. Relative particle number concentration was
405 defined by the estimated concentration with respect to the measured concentration. Values above 1 indicates
406 overestimation while values below 1 suggests underestimation. For approach 1 (FFNN-met), except for the overlapping
407 size bin, which are underestimated by more than 50% at all time range, the difference between estimated and measured
408 hourly number concentration is within 50% during both workdays and weekends. Overestimation is found in early
409 morning before 3 a.m. during workdays for all size bins, especially for UFP. Following the overestimation, at about 6
410 a.m. in the morning, the estimated number concentration appears to understate by up to 40%, especially at size bins below
411 $0.1 \mu\text{m}$. Along the day, the estimation uncertainties are rather small until in the evening from 6 p.m. to 11 p.m. where
412 estimated UFP number concentration show moderate overestimation one more time. It reveals that FFNN-met fails to
413 catch the diurnal pattern from 6 p.m. to 7 a.m. in particular for UFP. The pattern of the performance for weekends does
414 not appear to be as distinctive as on workdays. It shows the overestimation not only for UFP in early morning about 3
415 a.m., but also at the upper edge larger than $5 \mu\text{m}$ from 3 a.m. to 4 p.m.. At 7 p.m. onwards until noon, an underestimation

416 is found at all size bins. For approach 2 (FFNN-PSD), except the overlapping size bin, which has a significant
417 overestimation from 6 p.m. to 7 a.m., most show negligible 10% uncertainty during both workdays and weekends. The
418 performance over weekends show relatively stronger uncertainties. The smallest bin at 0.01 μm is slightly understated for
419 all hours of a day. Other than these, FFNN-PSD manages to catch fairly well the diurnal pattern for all size bins.

420

421 **Figure 11** ~~Figure 10~~ further shows the monthly deviation in estimation performance. For approach 1 (FFNN-met), higher R^2 is
422 found in November, February and April in the range of SMPS. Other than that, no observable variation in R^2 in approach
423 1 (FFNN-met). For approach 2 (FFNN-PSD), except in January when all the rows were eliminated because of the lack
424 of wind information, performance in the other months is steady for most size range. At 0.21 μm , the difference in
425 estimation performance varies across different months. R^2 in winter months are 0.76, 0.36 and 0.61, in November,
426 December and February, respectively, while R^2 exceeds 0.9 in other months. This unexpectedly low R^2 only occurs in the
427 winter months at the overlapping size range. It can be speculated that the measurements by the two instruments differ in
428 a larger extent during winter. This might be attributed to sensor drift and a number of interference artefacts for particle
429 measurements associated with several factors, such as relative humidity, temperature and other gas-phase species, which
430 were demonstrated by several researchers (e.g. Lewis et al., 2016; Popoola et al., 2016). Another reason for the difference
431 in estimation performance can be that the percentage of complete rows in these months are lower than the other months.
432 The drop in data points might impose an influence to the estimation performance. Especially in June, at the few size bins
433 close to the larger edge, R^2 ranges from 0.9 to 0.7. Besides that, some low R^2 can be also found in individual month at
434 both edges of size range, which does not appear to show any patterns.

435

436 In short, the estimation ability for lower edge ($0.01 < D_p < 0.03 \mu\text{m}$) is found worse in both approaches. The performance
437 of the FFNN method in mid-range ($0.15 < D_p < 0.5 \mu\text{m}$) and upper edge ($6 < D_p < 10 \mu\text{m}$) are relatively worse for the
438 approach with other fractionated size bins as input variables according to the aforementioned statistical performance
439 indicators. All statistical estimation simulations are based on the previous history of relationships between the inputs and
440 outputs. As a result, the estimation simulations for different size ranges have significantly unique connections. The
441 approach by meteorological parameters considers only 6 predictor variables so the accuracy is lower than FFNN-PSD. It
442 might not seem surprising that the deviations between the measured and estimated size distribution were not substantial
443 ($R^2 > 0.97$, $\text{NRMSE} < 0.25$) because FFNN-PSD takes 22 other size bins as predictor variables. This, still, gives a clue
444 that the proposed FFNN method can provide adequate solutions to particle size distribution prognostic demands.
445 Furthermore, this FFNN method outperforms the other selected widely used methods in terms of its accuracy and
446 reliability. The estimation of certain bin size by other bin sizes can be thought of replacing 'negative' values in the raw
447 data by particle sizers, including SMPS we used in this paper. Instead of eliminating the negative values, they can be
448 estimated by other size bins with a high accuracy in order to keep the symmetry in data error distribution (Viskari et al.,
449 2012).

450 5 Conclusion

451 This paper presents the evaluation of imputation methods by means of feed-forward neural network (FFNN) for estimating
452 particle number concentration at various particulate size bins. Input predictors include a merged particle size distribution,
453 by a scanning mobility particle sizer (NanoSMPS) and an optical particle sizer (OPS), which covers size range from 0.01
454 to 10, and meteorological parameters, including temperature (Temp), relative humidity (RH), wind speed (WS), wind

455 direction (WD) and ambient pressure (P). The measurements were collected in an urban background region in Amman,
456 the capital of Jordan in the period of 1 Aug 2016–31 July 2017. The total number concentration ($1.70 \pm 1.26 \times 10^4 \text{ cm}^{-3}$) in
457 the measurement period show moderate seasonal variability owing to the more suppressed boundary layer (Teinilä et al.,
458 2019) and the elevated wood combustion (Hellén et al., 2017) in wintertime. Similar to many other urban environments,
459 the diurnal pattern observed in this study reflects the traffic activity, which has a more pronounced pattern during
460 workdays (Hussein et al., 2019). The amount of coarse particles is negligible in terms of number concentration but dust
461 episodes were found often in spring during the measurement period.

462
463 We proposed three approaches with different input variables: (1) only meteorological parameters, (2) only number
464 concentration at the remaining size bins, and (3) both of the above. We performed optimisation to obtain the optimal
465 configuration of the FFNN methods, which are two layers with 10–15 neurons, balancing the accuracy and the computing
466 resources. The 5-min averaged meteorological parameters give varying number concentration estimation for various size
467 bins ($R^2 = 0.22\text{--}0.58$), which is outperformed by hourly and daily averaged data ($R^2 = 0.66\text{--}0.77$), as demonstrated by
468 Zaidan et al. (2020). The methods using the number concentration at the remaining size bins, both with or without
469 meteorological data, show expected perfect performance ($R^2 > 0.97$). We also compared the FFNN methods with other
470 commonly used methods and the results highlight the high accuracy and reliability of methods by means of neural
471 networks.

472
473 Relatively poor performance of the proposed FFNN methods is found in three regions. At the lower edge ($0.01 < D_p < 0.02$
474 μm) and the upper edge ($6 < D_p < 10 \mu\text{m}$), the number of neighbouring size bins is limited and also the detection efficiency
475 by the corresponding instruments is lower compared to the other size bins. Another noticeable region ($0.15 < D_p < 0.5 \mu\text{m}$)
476 is the overlapping section measured by the two particle sizers and the reason is because of the deficiency of merging
477 algorithm. For all the above approaches, the poorer performance for smaller particles in the nucleation mode could be due
478 to the fact that it is more effectively removed from the atmosphere compared to other modes (Al-Dabbous et al., 2017).
479 An observable overestimation is also found in early morning for ultrafine particles followed by a distinct underestimation
480 before midday. A larger derivation between the measured and the estimated number concentration is found in the winter,
481 which might be caused by sensor drift and interference artefacts (e.g. Lewis et al., 2016; Popoola et al., 2016). Despite
482 the high number of input predictors, the good estimation performance provides an alternative method to fill up the negative
483 values in size distribution raw dataset, which often exist due to misconfiguration problems. Instead of removing the
484 factually impossible data point, this way of replacing negative numbers can maintain a symmetric distribution of errors
485 (Viskari et al., 2012) and minimise the uncertainties caused.

486 **Code/Data availability**

487 The code and data is available upon request.

488 **Author contribution**

489 TH and MZ designed the experiments and TH carried them out. PLF and OS developed the code of the proposed FFNN
490 methods. PLF prepared the manuscript with contributions from all co-authors.

491 **Competing interests**

492 The authors declare that they have no conflict of interest.

493 **Financial support**

494 The work is supported by MegaSense program, the City of Helsinki Innovation Fund, Business Finland, the European
495 Union through the Urban Innovative Action Healthy Outdoor Premises for Everyone (HOPE, project No. UIA03-240).
496 This research is also funded by the Scientific Research Support Fund (SRF, Project Number BAS-1-2-2015) at the
497 Jordanian Ministry of Higher Education and the Deanship of Academic Research (DAR, Project Number 1516) at the
498 University of Jordan. This research is part of a close collaboration between the University of Jordan and the Institute for
499 Atmospheric and Earth System Research (INAR/Physics, University of Helsinki) via ERC advanced Grant No. 742206,
500 the European Union's Horizon 2020 research and innovation program under Grant Agreement No. 654109, the Academy
501 of Finland Flagship funding (Project No. 337549), ERA-PLANET (www.era-planet.eu), trans-national project SMURBS
502 (www.smurbs.eu, Grant Agreement No. 689443) funded under the EU Horizon 2020 Framework Programme, and
503 Academy of Finland via the Center of Excellence in Atmospheric sciences and NanoBioMass (Project Number 1307537).

504 **References**

505 Ahmed, R., Robinson, R., and Mortimer, K.: The epidemiology of noncommunicable respiratory disease in sub-Saharan
506 Africa, the Middle East, and North Africa, *Malawi Med J*, 29, 203-211, <https://doi.org/10.4314/mmj.v29i2.24>, 2017.
507 Al-Dabbous, A. N., Kumar, P., and Khan, A. R.: Prediction of airborne nanoparticles at roadside location using a feed-
508 forward artificial neural network, *Atmos Pollut Res*, 8, 446-454, <https://doi.org/10.1016/j.apr.2016.11.004>, 2017.
509 Arhami, M., Shahne, M. Z., Hosseini, V., Haghghat, N. R., Lai, A. M., and Schauer, J. J.: Seasonal trends in the
510 composition and sources of PM_{2.5} and carbonaceous aerosol in Tehran, Iran, *Environ Pollut*, 239, 69-81,
511 <https://doi.org/10.1016/j.envpol.2018.03.111>, 2018.
512 Borgie, M., Ledoux, F., Dagher, Z., Verdin, A., Cazier, F., Courcot, L., Shirali, P., Greige-Gerges, H., and Courcot, D.:
513 Chemical characteristics of PM_{2.5-0.3} and PM_{0.3} and consequence of a dust storm episode at an urban site in Lebanon,
514 *Atmos Res*, 180, 274-286, <https://doi.org/10.1016/j.atmosres.2016.06.001>, 2016.
515 Cabaneros, S. M., Calautit, J. K., and Hughes, B. R.: A review of artificial neural network models for ambient air pollution
516 prediction, *Environ Modell Softw*, 119, 285-304, <https://doi.org/10.1016/j.envsoft.2019.06.014>, 2019.
517 Cai, R., Yang, D., Ahonen, L. R., Shi, L., Korhonen, F., Ma, Y., Hao, J., Petäjä, T., Zheng, J., Kangasluoma, J., and Jiang,
518 J.: Data inversion methods to determine sub-3 nm aerosol size distributions using the particle size magnifier, *Atmos Meas*
519 *Tech*, 11, 4477-4491, <https://doi.org/10.5194/amt-11-4477-2018>, 2018.
520 Chaloulakou, A., Grivas, G., and Spyrellis, N.: Neural network and multiple regression models for PM₁₀ prediction in
521 Athens: a comparative assessment, *J Air Waste Manag Assoc*, 53, 1183-1190,
522 <https://doi.org/10.1080/10473289.2003.10466276>, 2003.
523 DeCarlo, P. F., Slowik, J. G., Worsnop, D. R., Davidovits, P., and Jimenez, J. L.: Particle morphology and density
524 characterization by combined mobility and aerodynamic diameter measurements. Part 1: Theory, *Aerosol Sci Tech*, 38,
525 1185-1205, <https://doi.org/10.1080/027868290903907>, 2004.
526 Enting, I., and Newsam, G.: Atmospheric constituent inversion problems: Implications for baseline monitoring, *J Atmos*
527 *Chem*, 11, 69-87, <https://doi.org/10.1007/BF00053668>, 1990.
528 Fonseca, A. S., Viana, M., Perez, N., Alastuey, A., Querol, X., Kaminski, H., Todea, A. M., Monz, C., and Asbach, C.:
529 Intercomparison of a portable and two stationary mobility particle sizers for nanoscale aerosol measurements, *Aerosol*
530 *Sci Tech*, 50, 653-668, <https://doi.org/10.1080/02786826.2016.1174329>, 2016.
531 Freeman, B. S., Taylor, G., Gharabaghi, B., and Thé, J.: Forecasting air quality time series using deep learning, *J Air*
532 *Waste Manag Assoc*, 68, 866-886, <https://doi.org/10.1080/10962247.2018.1459956>, 2018.
533 Fung, P. L., Zaidan, M. A., Timonen, H., Niemi, J. V., Kousa, A., Kuula, J., Luoma, K., Tarkoma, S., Petäjä, T., Kulmala,
534 M., and Hussein, T.: Evaluation of white-box versus black-box machine learning models in estimating ambient black
535 carbon concentration, *J Aerosol Sci*, <https://doi.org/10.1016/j.jaerosci.2020.105694>, 2020.
536 Gherboudj, I., Beegum, S. N., and Ghedira, H.: Identifying natural dust source regions over the Middle-East and North-
537 Africa: Estimation of dust emission potential, *Earth-Sci Rev*, 165, 342-355,
538 <https://doi.org/10.1016/j.earscirev.2016.12.010>, 2017.

539 Goudarzi, G., Shirmardi, M., Naimabadi, A., Ghadiri, A., and Sajedifar, J.: Chemical and organic characteristics of PM_{2.5}
540 particles and their in-vitro cytotoxic effects on lung cells: The Middle East dust storms in Ahvaz, Iran, *Sci Total Environ*,
541 655, 434-445, <https://doi.org/10.1016/j.scitotenv.2018.11.153>, 2019.

542 Gupta, R., and Xie, H.: Nanoparticles in Daily Life: Applications, Toxicity and Regulations, *J Environ Pathol Toxicol*
543 *Oncol*, 37, 209-230, <https://doi.org/10.1615/JEnvironPatholToxicolOncol.2018026009>, 2018.

544 Hakala, S., Alghamdi, M. A., Paasonen, P., Vakkari, V., Khoder, M. I., Neitola, K., Dada, L., Abdelmaksoud, A. S., Al-
545 Jeelani, H., Shabbaj, I. I., Almeahadi, F. M., Sundström, A. M., Lihavainen, H., Kerminen, V. M., Kontkanen, J.,
546 Kulmala, M., Hussein, T., and Hyvärinen, A. P.: New particle formation, growth and apparent shrinkage at a rural
547 background site in western Saudi Arabia, *Atmos Chem Phys*, 19, 10537-10555, [https://doi.org/10.5194/acp-19-10537-](https://doi.org/10.5194/acp-19-10537-2019)
548 [2019](https://doi.org/10.5194/acp-19-10537-2019), 2019.

549 Hellén, H., Kangas, L., Kousa, A., Vestenius, M., Teinilä, K., Karppinen, A., Kukkonen, J., and Niemi, J. V.: Evaluation
550 of the impact of wood combustion on benzo[a]pyrene (BaP) concentrations; ambient measurements and dispersion
551 modeling in Helsinki, Finland, *Atmos Chem Phys*, 17, 3475-3487, <https://doi.org/10.5194/acp-17-3475-2017>, 2017.

552 Hussein, T., Dal Maso, M., Petäjä, T., Koponen, I. K., Paatero, P., Aalto, P. P., Hämeri, K., and Kulmala, M.: Evaluation
553 of an automatic algorithm for fitting the particle number size distributions, *Boreal Environ Res*, 10, 337-355, 2005.

554 Hussein, T., Dada, L., Hakala, S., Petäjä, T., and Kulmala, M.: Urban Aerosol Particle Size Characterization in Eastern
555 Mediterranean Conditions, *Atmosphere*, 10, <https://doi.org/10.3390/atmos10110710>, 2019.

556 Hussein, T., Atashi, N., Sogacheva, L., Hakala, S., Dada, L., Petäjä, T., and Kulmala, M.: Characterization of Urban New
557 Particle Formation in Amman—Jordan, *Atmosphere*, 11, <https://doi.org/10.3390/atmos11010079>, 2020.

558 Junger, W., and Ponce De Leon, A.: Imputation of missing data in time series for air pollutants, *Atmos Environ*, 102, 96-
559 104, <https://doi.org/10.1016/j.atmosenv.2014.11.049>, 2015.

560 Kandlikar, M., and Ramachandran, G.: Inverse methods for analysing aerosol spectrometer measurements: a critical
561 review, *J Aerosol Sci*, 30, 413-437, [https://doi.org/10.1016/S0021-8502\(98\)00066-4](https://doi.org/10.1016/S0021-8502(98)00066-4), 1999.

562 Kannosto, J., Virtanen, A., Lemmetty, M., Mäkelä, J. M., Keskinen, J., Junninen, H., Hussein, T., Aalto, P., and Kulmala,
563 M.: Mode resolved density of atmospheric aerosol particles, *Atmos Chem Phys*, 8, 5327-5337,
564 <https://doi.org/10.5194/acp-8-5327-2008>, 2008.

565 Kerminen, V. M., Paramonov, M., Anttila, T., Riipinen, I., Fountoukis, C., Korhonen, H., Asmi, E., Laakso, L.,
566 Lihavainen, H., Swietlicki, E., Svenningsson, B., Asmi, A., Pandis, S. N., Kulmala, M., and Petaja, T.: Cloud
567 condensation nuclei production associated with atmospheric nucleation: a synthesis based on existing literature and new
568 results, *Atmos Chem Phys*, 12, 12037-12059, <https://doi.org/10.5194/acp-12-12037-2012>, 2012.

569 Kerminen, V. M., Chen, X. M., Vakkari, V., Petaja, T., Kulmala, M., and Bianchi, F.: Atmospheric new particle formation
570 and growth: review of field observations, *Environ Res Lett*, 13, <https://doi.org/10.1088/1748-9326/aadf3c>, 2018.

571 Kok, J. F., Ridley, D. A., Zhou, Q., Miller, R. L., Zhao, C., Heald, C. L., Ward, D. S., Albani, S., and Hausteine, K.:
572 Smaller desert dust cooling effect estimated from analysis of dust size and abundance, *Nat Geosci*, 10, 274-278,
573 <https://doi.org/10.1038/Ngeo2912>, 2017.

574 Kreyling, W. G., Semmler, M., and Moller, W.: Dosimetry and toxicology of ultrafine particles, *J Aerosol Med*, 17, 140-
575 152, <https://doi.org/10.1089/0894268041457147>, 2004.

576 Kulkarni, P., Baron, P. A., and Willeke, K.: *Aerosol measurement: principles, techniques, and applications*, John Wiley
577 & Sons, 2011.

578 Kulmala, M., Vehkamäki, H., Petaja, T., Dal Maso, M., Lauri, A., Kerminen, V. M., Birmili, W., and McMurry, P. H.:
579 Formation and growth rates of ultrafine atmospheric particles: a review of observations, *J Aerosol Sci*, 35, 143-176,
580 <https://doi.org/10.1016/j.jaerosci.2003.10.003>, 2004.

581 Laakso, L., Hussein, T., Aarnio, P., Komppula, M., Hiltunen, V., Viisanen, Y., and Kulmala, M.: Diurnal and annual
582 characteristics of particle mass and number concentrations in urban, rural and Arctic environments in Finland, *Atmos*
583 *Environ*, 37, 2629-2641, [https://doi.org/10.1016/S1352-2310\(03\)00206-1](https://doi.org/10.1016/S1352-2310(03)00206-1), 2003.

584 Lehtipalo, K., Leppä, J., Kontkanen, J., Kangasluoma, J., Franchin, A., Wimmer, D., Schobesberger, S., Junninen, H.,
585 Petaja, T., Sipilä, M., Mikkilä, J., Vanhanen, J., Worsnop, D. R., and Kulmala, M.: Methods for determining particle size
586 distribution and growth rates between 1 and 3 nm using the Particle Size Magnifier, *Boreal Environ Res*, 2014.

587 Lelieveld, J., Evans, J. S., Fnais, M., Giannadaki, D., and Pozzer, A.: The contribution of outdoor air pollution sources to
588 premature mortality on a global scale, *Nature*, 525, 367-371, <https://doi.org/10.1038/nature15371>, 2015.

589 Lewis, A. C., Lee, J. D., Edwards, P. M., Shaw, M. D., Evans, M. J., Moller, S. J., Smith, K. R., Buckley, J. W., Ellis,
590 M., Gillot, S. R., and White, A.: Evaluating the performance of low cost chemical sensors for air pollution research,
591 *Faraday Discuss*, 189, 85-103, <https://doi.org/10.1039/c5fd00201j>, 2016.

592 Liu, Z. R., Hu, B., Liu, Q., Sun, Y., and Wang, Y. S.: Source apportionment of urban fine particle number concentration
593 during summertime in Beijing, *Atmos Environ*, 96, 359-369, <https://doi.org/10.1016/j.atmosenv.2014.06.055>, 2014.

594 Londaal, J., Moller, W., Pagels, J. H., Kreyling, W. G., Swietlicki, E., and Schmid, O.: Measurement techniques for
595 respiratory tract deposition of airborne nanoparticles: a critical review, *J Aerosol Med Pulm Drug Deliv*, 27, 229-254,
596 <https://doi.org/10.1089/jamp.2013.1044>, 2014.

597 Maleki, H., Sorooshian, A., Goudarzi, G., Baboli, Z., Birgani, Y. T., and Rahmati, M.: Air pollution prediction by using
598 an artificial neural network model, *Clean Technol Environ Policy*, 21, 1341–1352, <https://doi.org/10.1007/s10098-019-01709-w>, 2019.

599
600 Markowski, G. R.: Improving Twomey's algorithm for inversion of aerosol measurement data, *Aerosol Sci Tech*, 7, 127-
601 141, <https://doi.org/10.1080/02786828708959153>, 1987.

602 Morawska, L., Ristovski, Z., Jayaratne, E. R., Keogh, D. U., and Ling, X.: Ambient nano and ultrafine particles from
603 motor vehicle emissions: Characteristics, ambient processing and implications on human exposure, *Atmos Environ*, 42,
604 8113-8138, <https://doi.org/10.1016/j.atmosenv.2008.07.050>, 2008.

605 Ohlwein, S., Kappeler, R., Joss, M. K., Kunzli, N., and Hoffmann, B.: Health effects of ultrafine particles: a systematic
606 literature review update of epidemiological evidence, *Int J Public Health*, 64, 547-559, <https://doi.org/10.1007/s00038-019-01202-7>, 2019.

607
608 Popoola, O. A. M., Stewart, G. B., Mead, M. I., and Jones, R. L.: Development of a baseline-temperature correction
609 methodology for electrochemical sensors and its implications for long-term stability, *Atmos Environ*, 147, 330-343,
610 <https://doi.org/10.1016/j.atmosenv.2016.10.024>, 2016.

611 Rönkkö, T., Kuuluvainen, H., Karjalainen, P., Keskinen, J., Hillamo, R., Niemi, J. V., Pirjola, L., Timonen, H. J.,
612 Saarikoski, S., Saukko, E., Jarvinen, A., Silvennoinen, H., Rostedt, A., Olin, M., Yli-Ojanpera, J., Nousiainen, P., Kousa,
613 A., and Dal Maso, M.: Traffic is a major source of atmospheric nanocluster aerosol, *P Natl Acad Sci USA*, 114, 7549-
614 7554, <https://doi.org/10.1073/pnas.1700830114>, 2017.

615 Spinazzè, A., Fantì, G., Borghi, F., Del Buono, L., Campagnolo, D., Rovelli, S., Cattaneo, A., and Cavallo, D. M.: Field
616 comparison of instruments for exposure assessment of airborne ultrafine particles and particulate matter, *Atmos Environ*,
617 154, 274-284, <https://doi.org/10.1016/j.atmosenv.2017.01.054>, 2017.

618 Stolzenburg, M. R., and McMurry, P. H.: Method to assess performance of scanning mobility particle sizer (SMPS)
619 instruments and software, *Aerosol Sci Tech*, 52, 609-613, <https://doi.org/10.1080/02786826.2018.1455962>, 2018.

620 Teinilä, K., Aurela, M., Niemi, J. V., Kousa, A., Petäjä, T., Järvi, L., Hillamo, R., Kangas, L., Saarikoski, S., and Timonen,
621 H.: Concentration variation of gaseous and particulate pollutants in the Helsinki city centre — observations from a two-
622 year campaign from 2013–2015, *Boreal Environ Res*, 24, 115–136, 2019.

623 Tritscher, T., Beeston, M., Zerrath, A. F., Elzey, S., Krinke, T. J., Filimundi, E., and Bischof, O. F.: NanoScan SMPS -
624 A Novel, Portable Nanoparticle Sizing and Counting Instrument, *J Phys: Conf Ser*, 429, 012061,
625 <https://doi.org/10.1088/1742-6596/429/1/012061>, 2013.

626 Tritscher, T., Koched, A., Han, H. S., Filimundi, E., Johnson, T., Elzey, S., Avenido, A., Kykal, C., and Bischof, O. F.:
627 Multi-Instrument Manager Tool for Data Acquisition and Merging of Optical and Electrical Mobility Size Distributions,
628 *J Phys: Conf Ser*, 617, 012013, <https://doi.org/10.1088/1742-6596/617/1/012013>, 2015.

629 Viskari, T., Asmi, E., Kolmonen, P., Vuollekoski, H., Petaja, T., and Jarvinen, H.: Estimation of aerosol particle number
630 distributions with Kalman Filtering - Part I: Theory, general aspects and statistical validity, *Atmos Chem Phys*, 12, 11767-
631 11779, <https://doi.org/10.5194/acp-12-11767-2012>, 2012.

632 Wiedensohler, A., Birmili, W., Nowak, A., Sonntag, A., Weinhold, K., Merkel, M., Wehner, B., Tuch, T., Pfeifer, S.,
633 Fiebig, M., Fjåraa, A. M., Asmi, E., Sellegri, K., Depuy, R., Venzac, H., Villani, P., Laj, P., Aalto, P., Ogren, J. A.,
634 Swietlicki, E., Williams, P., Roldin, P., Quincey, P., Hüglin, C., Fierz-Schmidhauser, R., Gysel, M., Weingartner, E.,
635 Riccobono, F., Santos, S., Gröning, C., Faloon, K., Beddows, D., Harrison, R., Monahan, C., Jennings, S. G., O'Dowd,
636 C. D., Marinoni, A., Horn, H. G., Keck, L., Jiang, J., Scheckman, J., McMurry, P. H., Deng, Z., Zhao, C. S., Moerman,
637 M., Henzing, B., de Leeuw, G., Löschau, G., and Bastian, S.: Mobility particle size spectrometers: harmonization of
638 technical standards and data structure to facilitate high quality long-term observations of atmospheric particle number
639 size distributions, *Atmos Meas Tech*, 5, 657-685, <https://doi.org/10.5194/amt-5-657-2012>, 2012.

640 Population growth (annual %): <https://data.worldbank.org/indicator/SP.POP.GROW>, access: 06-10, 2019.

641 World Health Organisation: World health statistics 2019: Monitoring health for the SDGs, sustainable development goals,
642 World Health Organisation, <https://apps.who.int/iris/handle/10665/324835>, 2019.

643 Xing, Y. F., Xu, Y. H., Shi, M. H., and Lian, Y. X.: The impact of PM2.5 on the human respiratory system, *J Thorac Dis*,
644 8, E69-74, <https://doi.org/10.3978/j.issn.2072-1439.2016.01.19>, 2016.

645 Zaidan, M. A., Canova, F. F., Laurson, L., and Foster, A. S.: Mixture of Clustered Bayesian Neural Networks for
646 Modeling Friction Processes at the Nanoscale, *J Chem Theory Comput*, 13, 3-8, <https://doi.org/10.1021/acs.jctc.6b00830>,
647 2017.

648 Zaidan, M. A., Surakhi, O., Fung, P. L., and Hussein, T.: Sensitivity Analysis for Predicting Sub-Micron Aerosol
649 Concentrations Based on Meteorological Parameters, *Sensors (Basel)*, 20, <https://doi.org/10.3390/s20102876>, 2020.

650 Zhou, Y., Dada, L., Liu, Y., Fu, Y., Kangasluoma, J., Chan, T., Yan, C., Chu, B., Daellenbach, K. R., Bianchi, F.,
651 Kokkonen, T. V., Liu, Y., Kujansuu, J., Kerminen, V.-M., Petäjä, T., Wang, L., Jiang, J., and Kulmala, M.: Variation of
652 size-segregated particle number concentrations in wintertime Beijing, *Atmos Chem Phys*, 20, 1201-1216,
653 <https://doi.org/10.5194/acp-20-1201-2020>, 2020.

654

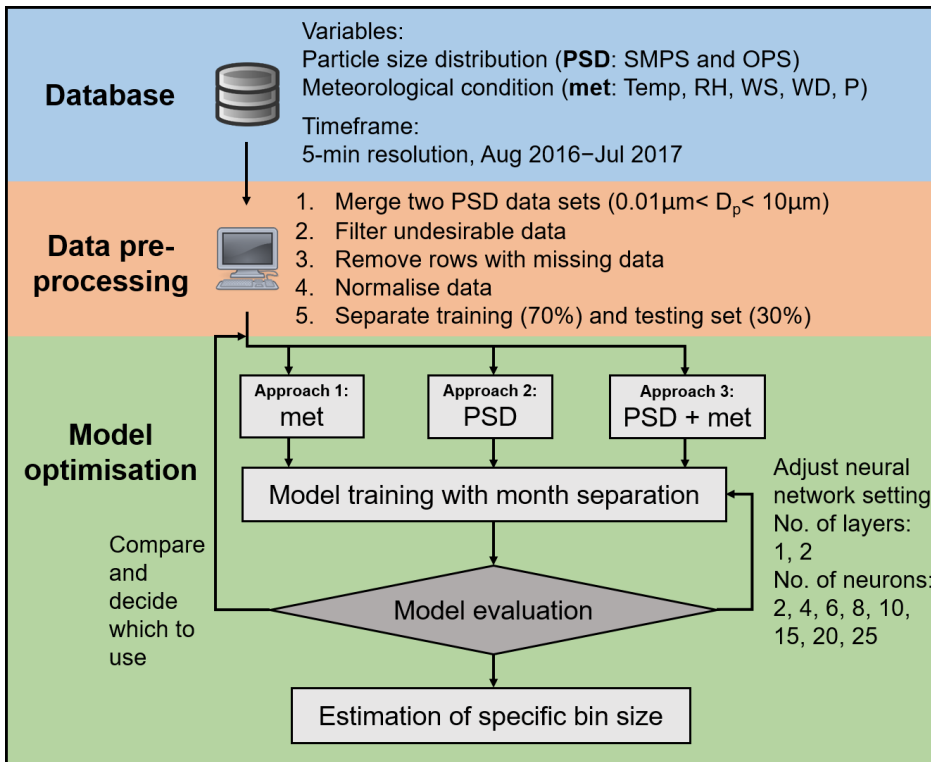


Figure 1. The block diagram describing the methodology of the proposed FFNN method.

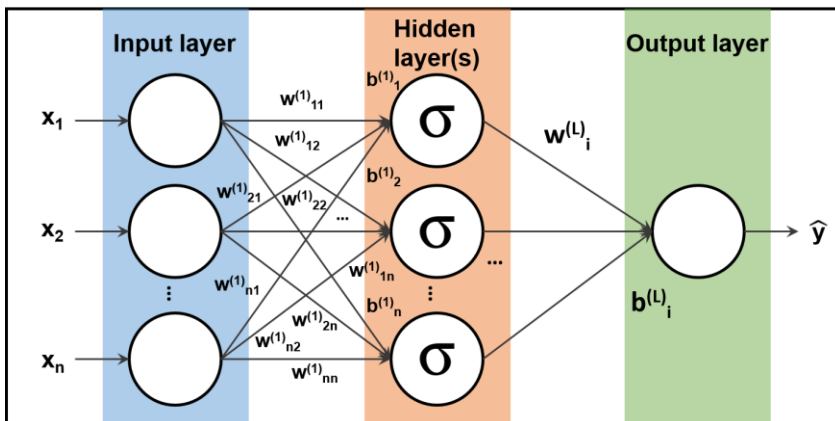


Figure 2. Schematic diagram of a neural network with one hidden layer of sigmoid activation function.

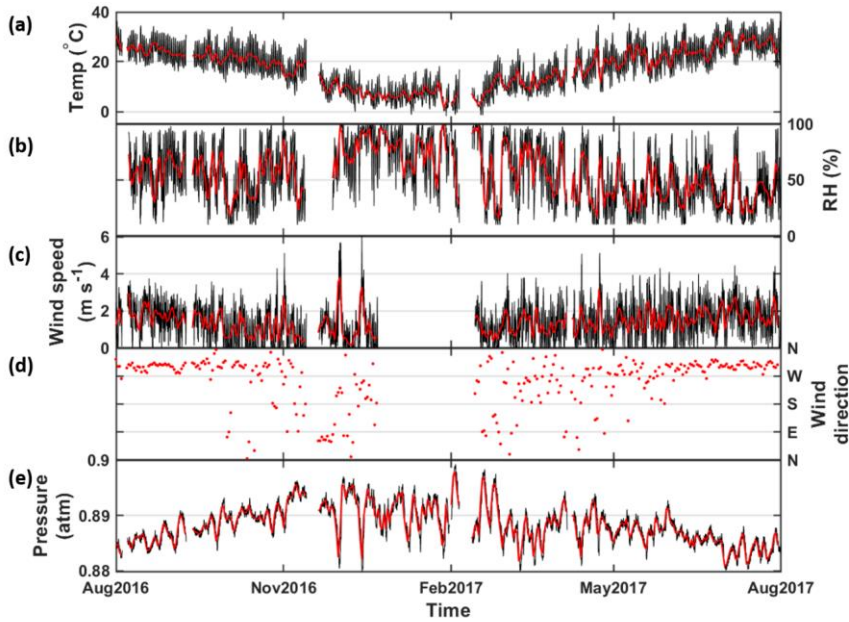


Figure 3. Timeseries of meteorological conditions during the measurement period Aug 2016–Jul 2017. (a–e) denotes temperature, relative humidity, wind speed, wind direction and air pressure, respectively. Black and red represent hourly and daily averaged data, respectively.

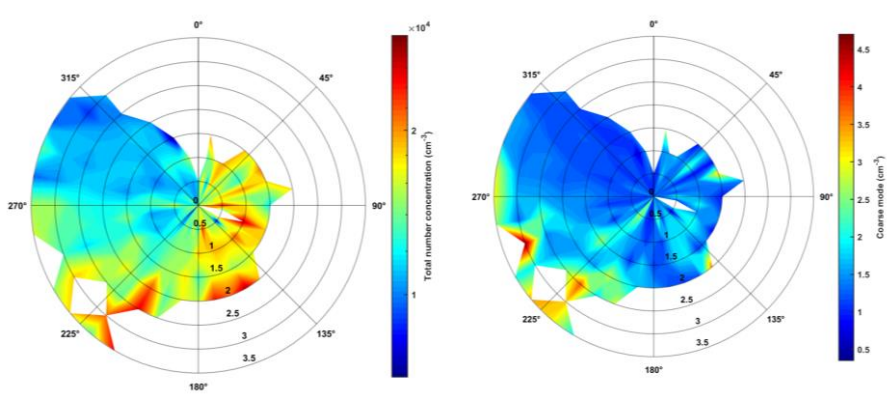


Figure 4. Windrose diagram of total particle number concentration at different direction (in theta axis) and different wind speed (in radial axis). Wind direction and wind speed data are grouped in every 10° and 0.5 m s^{-1} . Warmer color represent higher total particle number concentration. (a) total number concentration, log scale; (b) coarse mode, linear scale. Note the color scales are different.

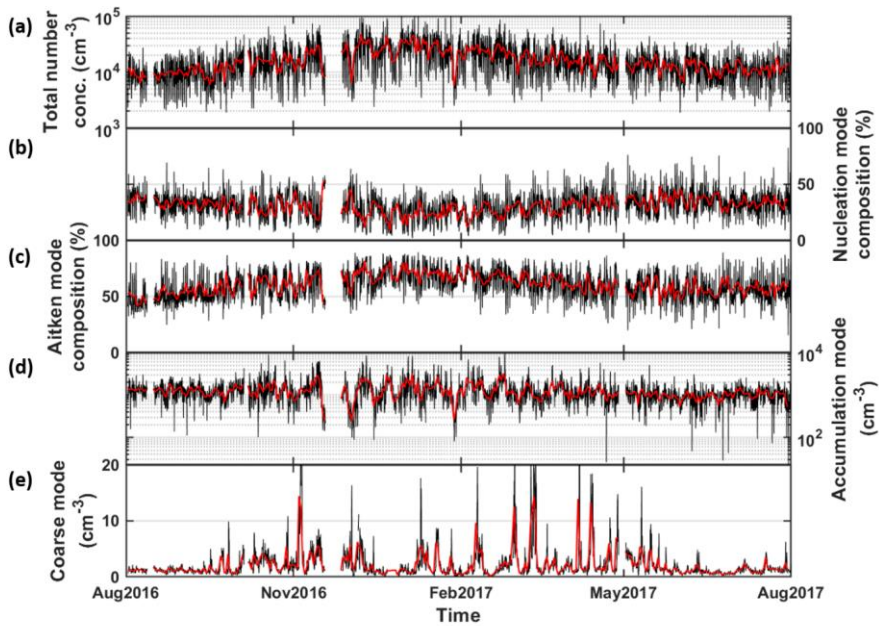


Figure 5. Timeseries of total particle number concentration (in cm^{-3}) of $0.01\text{--}10\mu\text{m}$ in (a). (b–c) indicate the contribution in percentage of nucleation mode and Aitken mode, respectively. (d–e) show the number concentration in accumulation mode and coarse mode, respectively. Black and red represent hourly and daily averaged data, respectively.

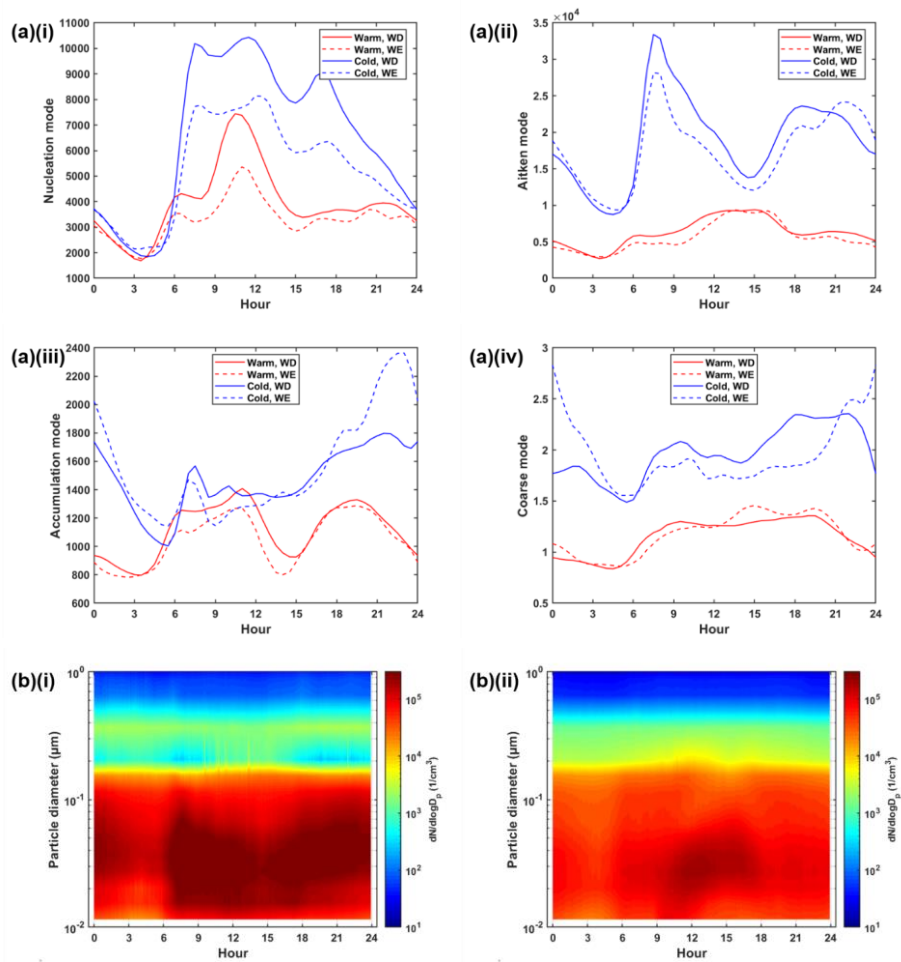


Figure 6. (a) Diurnal cycle of the (i) nucleation mode, (ii) Aitken mode, (iii) accumulation mode and (iv) coarse mode in warm (red) and cold months (blue) during workdays (solid) and weekends (dashed). (b) Particle size distribution in (i) cold and (ii) warm months, coloured by particle number concentration (cm^{-3}). Cold and warm months refer to December–February and June–August, respectively.

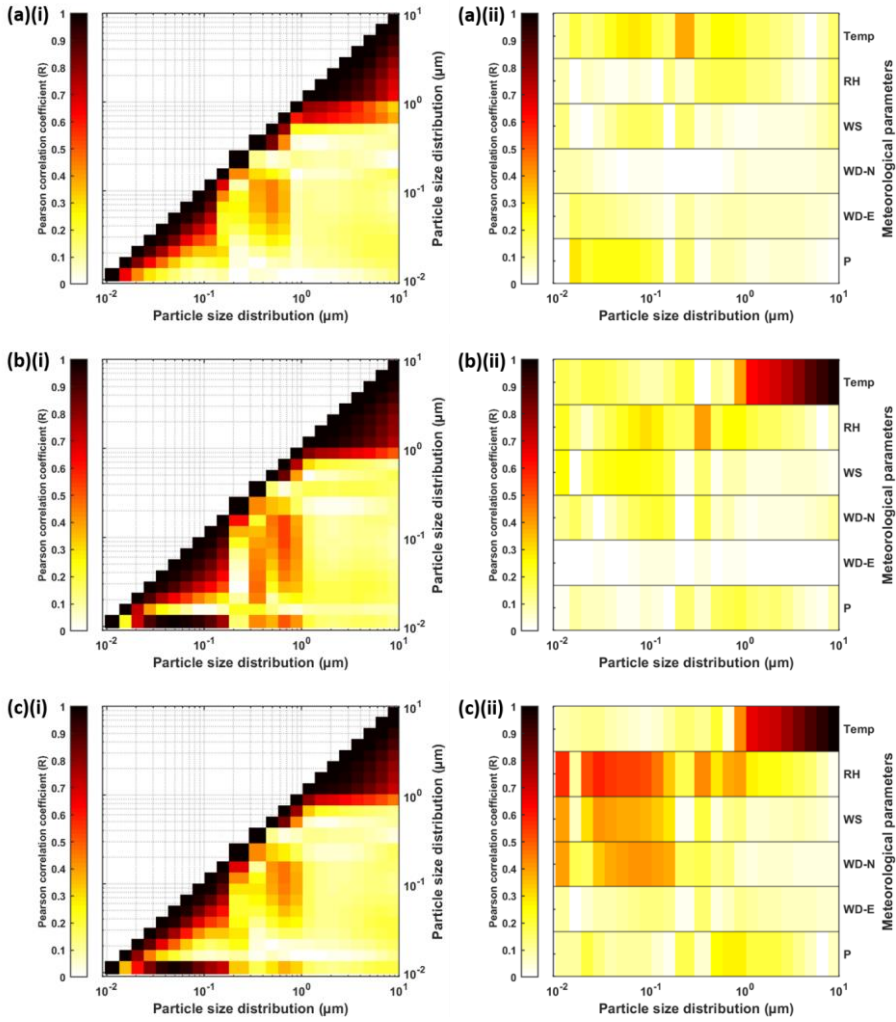
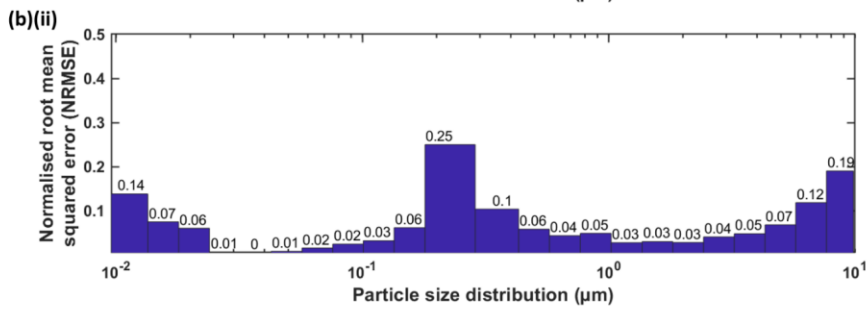
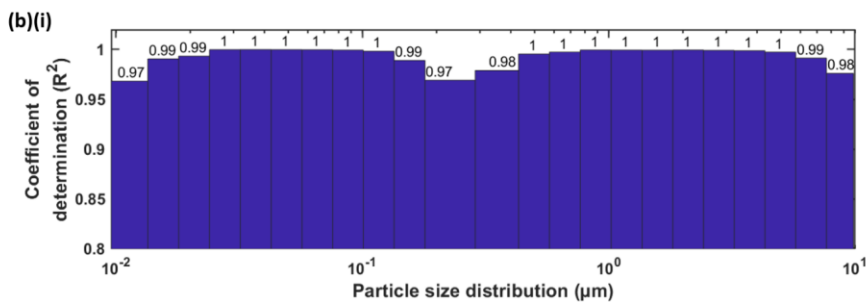
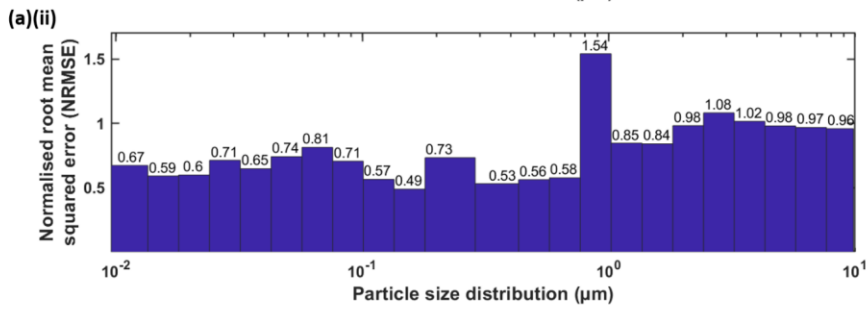
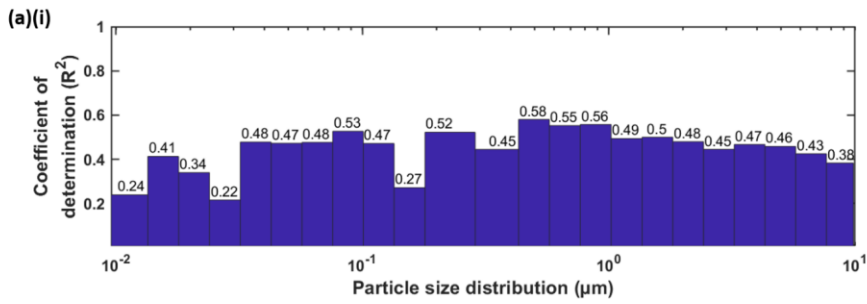


Figure 7. Matrix plots showing the Pearson correlation coefficient (R) of particle size distribution of (a) 5-min, (b) hourly, (c) daily averaging with (i) particle size distribution itself and (ii) meteorological parameters. Darker colour represents a higher correlation.



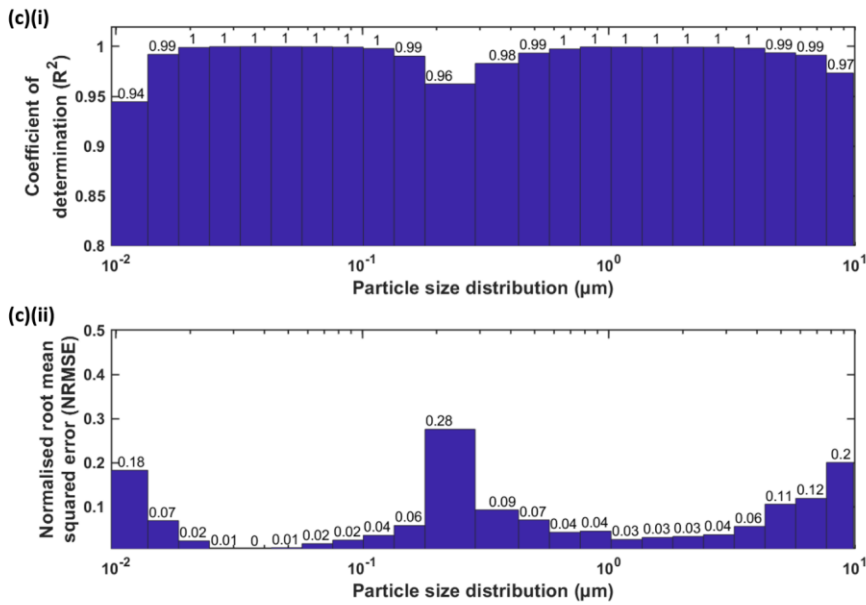


Figure 8. Bar chart showing the evaluation of FFNN approach with (a) only meteorological parameters (Approach 1, FFNN-met), (b) particle size distribution itself (Approach 2, FFNN-PSD), (c) both particle size distribution and meteorological parameters (Approach 3) as inputs. The evaluation metrics for the proposed method include (i) coefficient of determination (R²) and (ii) normalised root mean squared error (NRMSE).

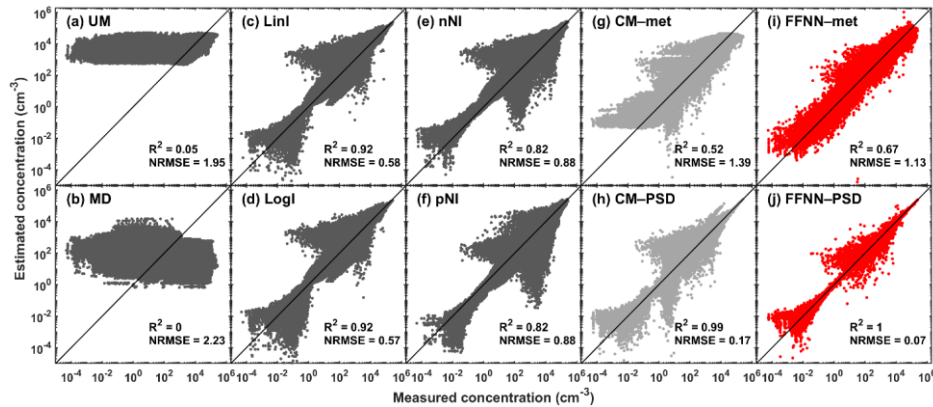


Figure 9. Scatter plots showing the estimated particle concentration (y-axis, in cm⁻³) against the measured in situ particle concentration (x-axis, in cm⁻³). (a-f) demonstrate cases of univariate methods including unconditional mean (UM), median (MD), linear interpolation (LinI), logarithmic interpolation (LogI), next neighbour interpolation (nNI) and previous neighbour interpolation (pNI), respectively, in dark grey dots. (g-h) represent multivariate methods conditional mean by regression of meteorological parameters and other particle size number concentrations as inputs (CM-met and CM-PSD, respectively) in light grey dots. (i-j) showcase the proposed feed-forward neural network with meteorological parameters and other particle size number concentrations as inputs (FFNN-met and FFNN-PSD, respectively) in red dots. The black solid line is 1:1 line which gives a reference of perfect estimation. The coefficient

Formatted: Font: Not Italic

Formatted: Font: Not Italic

Formatted: Font: Not Italic

Formatted: Superscript

Formatted: Superscript

Formatted: Font: Not Italic

of determination (R^2) and the normalised root-mean-square error (NRMSE) of each method for all particle size bins are printed on the corresponding subplots.

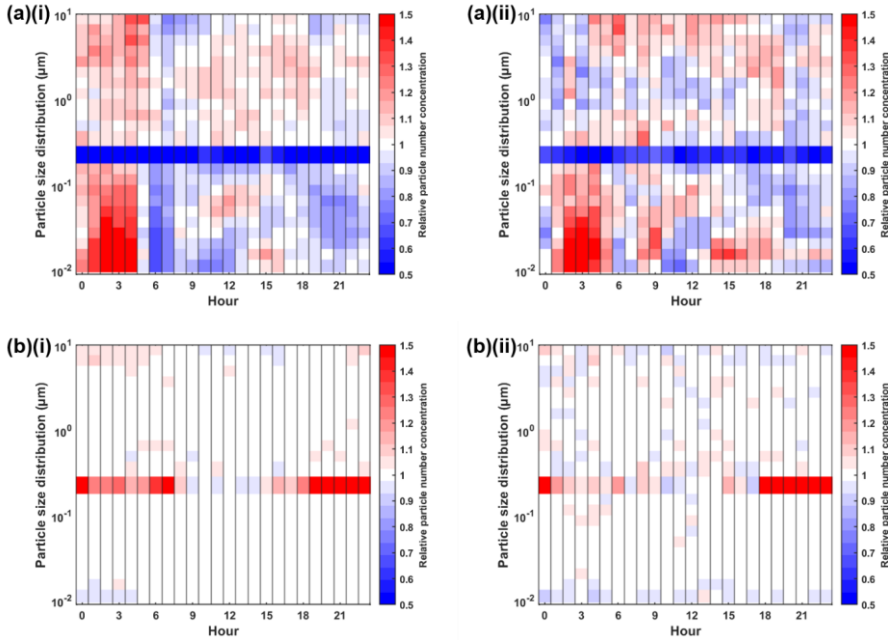


Figure 109. Heatmap showing the hourly median relative particle number concentration of the approach with (a) meteorological parameters (Approach 1, FFNN-met) and (b) particle size distribution (Approach 2, FFNN-PSD) as inputs across different hours of a day (i) in workdays and (ii) in weekends. The relative particle number concentration is defined as estimated concentration with respect to measured concentration. Red colour show overestimation while blue show underestimation.

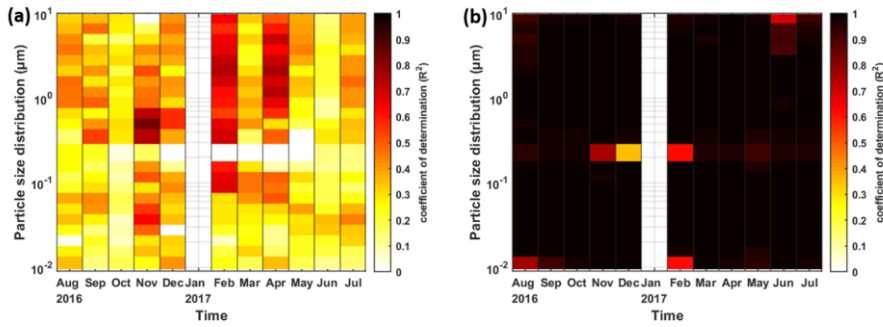


Figure 114. Heatmap showing the coefficient of determination (R^2) of the approach with (a) meteorological parameters (Approach 1, FFNN-met) and (b) particle size distribution (Approach 2, FFNN-PSD) as inputs for different months at different size bins. Darker colour represents a higher R^2 .

656 Table 1. Table showing the descriptive statistics (in cm^{-3}) of total number concentration, nucleation mode, Aitken mode,
 657 accumulation mode and coarse mode. The statistical values include mean, standard deviation, and percentile (10%, 25%,
 658 50%, 75% and 90%).

	Mean	std	10%	25%	50%	75%	90%
Total ($\times 10^4$)	1.70	1.26	0.57	0.85	1.35	2.16	3.31
Nucleation ($\times 10^4$)	0.48	0.32	0.16	0.26	0.41	0.63	0.90
Aitken ($\times 10^4$)	1.09	1.01	0.29	0.45	0.77	1.37	2.35
Accumulation ($\times 10^4$)	0.13	0.08	0.05	0.08	0.11	0.15	0.21
Coarse	2.13	2.80	0.55	0.84	1.29	2.33	4.3

659 Table 2. Table showing the best configuration in the form of (the number of layers; the number of neurons) for the
 660 approach by meteorological parameters (FFNN-met) and the number concentration at the other size bins (FFNN-PSD)
 661 as inputs. Mean absolute error (MAE, in cm^{-3}), coefficient of determination (R^2) and normalised root-mean-square error
 662 (NRMSE) are listed for different size bins on each row. The last row concludes the overall selection of the approach with
 663 the best configuration and its corresponding evaluation metrics.
 664

Particle size (μm)	Approach 1 (FFNN-met)				Approach 2 (FFNN-PSD)			
	Best setting	MAE (cm^{-3})	R^2	NRMSE	Best setting	MAE (cm^{-3})	R^2	NRMSE
0.012	2; 10	2640	0.20	0.69	2; 10	334	0.99	0.11
0.015	2; 15	4850	0.42	0.59	2; 8	216	1.00	0.031
0.021	2; 15	6120	0.38	0.58	2; 15	97.8	1.00	0.014
0.027	2; 15	8470	0.41	0.62	1; 25	34.0	1.00	0.0032
0.037	2; 20	8240	0.46	0.66	2; 15	26.3	1.00	0.0024
0.049	2; 15	6610	0.48	0.74	2; 25	33.7	1.00	0.0049
0.066	2; 15	4690	0.46	0.83	2; 10	56.7	1.00	0.013
0.088	2; 15	3040	0.52	0.71	2; 4	66.2	1.00	0.018
0.12	2; 15	1810	0.52	0.54	2; 8	63.1	1.00	0.021
0.15	2; 10	917	0.29	0.49	2; 15	72.5	0.99	0.052
0.21	2; 6	327	0.55	0.71	2; 8	114	0.91	0.31
0.37	2; 10	95.8	0.43	0.54	2; 20	12.9	0.99	0.072
0.49	2; 15	12.1	0.50	0.61	2; 25	0.9630	1.00	0.043
0.66	2; 15	3.03	0.58	0.56	2; 15	0.1995	1.00	0.029
0.88	2; 15	5.65	0.62	1.43	2; 10	0.2202	1.00	0.040
1.17	2; 15	1.43	0.53	0.81	2; 8	0.0680	1.00	0.026
1.56	2; 20	1.44	0.54	0.81	2; 8	0.0816	1.00	0.031
2.08	2; 15	1.84	0.49	0.97	2; 8	0.0825	1.00	0.028
2.77	2; 15	1.02	0.44	1.09	1; 4	0.0573	1.00	0.037
3.70	2; 15	0.52	0.41	1.07	1; 8	0.0329	1.00	0.046
4.92	2; 15	0.28	0.44	1.00	1; 4	0.0254	1.00	0.068
6.56	2; 9	0.11	0.42	0.97	1; 6	0.0206	0.99	0.13
8.75	2; 10	0.060	0.39	0.95	2; 6	0.0169	0.98	0.20
overall	2; 15	2120	0.67	1.13	2; 10	76.6	0.999	0.067

666 Table 3. Table showing the comparison of different estimation methods, including unconditional mean (UM, column 2),
667 median (MD, column 3), linear interpolation (LinI, column 4), logarithmic interpolation (LogI, column 5), next neighbour
668 interpolation (nNI, column 6), previous neighbour interpolation (pNI, column 7), conditional mean by regression of
669 meteorological parameters and other particle size number concentrations as inputs (CM—met and CM—PSD, column 8
670 and 9, respectively) and the feed-forward neural network with meteorological parameters and other particle size number
671 concentrations as inputs (FFNN—met and FFNN—PSD, column 10 and 11, respectively). The coefficient of
672 determination (R^2) of each method are listed for different size bins on each row. Negative R^2 are represented as '0' to
673 indicate poor accuracy at the particular particle size bin while 'NA' is used to represent the data is not available. The last
674 row concludes the overall evaluation metrics.

Particle size (μm)	Methods/ R^2									
	UM	MD	LinI	LogI	nNI	pNI	CM —met	CM —PSD	FFNN —met	FFNN —PSD
0.012	0	0	0	0	1.00	NA	0.04	0.91	0.20	0.99
0.015	0	0	0.66	0.71	0	0.49	0.14	0.85	0.42	1.00
0.021	0	0	0.92	0.91	0.62	0.33	0.1	1.00	0.38	1.00
0.027	0	0	0.91	0.93	0.69	0.90	0.11	1.00	0.41	1.00
0.037	0	0	0.97	0.97	0.91	0.85	0.12	1.00	0.46	1.00
0.049	0	0	0.98	0.99	0.80	0.80	0.13	1.00	0.48	1.00
0.066	0.14	0	0.96	0.97	0.66	0.81	0.14	1.00	0.46	1.00
0.088	0.31	0	0.97	0.98	0.60	0.64	0.12	1.00	0.52	1.00
0.12	0.41	0	0.92	0.96	0	0	0.07	1.00	0.52	1.00
0.15	0	0	0	0.20	0	0	0.03	0.97	0.29	0.99
0.21	0	0	0	0	0	0	0.24	0.65	0.55	0.91
0.37	0	0	0	0	0	0	0.04	0.9	0.43	0.99
0.49	0	0	0	0	0	0	0.06	0.97	0.50	1.00
0.66	0	0	0	0	0	0	0.07	0.96	0.58	1.00
0.88	0	0	0.20	0.19	0.23	0.11	0.09	0.76	0.62	1.00
1.17	0	0	0	0	0	0.99	0.04	1.00	0.53	1.00
1.56	0	0	0.97	0.97	0.99	0.85	0.04	1.00	0.54	1.00
2.08	0	0	0.84	0.83	0.91	0.67	0.03	1.00	0.49	1.00
2.77	0	0	0.90	0.96	0	0.60	0.02	1.00	0.44	1.00
3.70	0	0	0.76	0.87	0	0.62	0.02	1.00	0.41	1.00
4.92	0	0	0.85	0.94	0	0.41	0.02	1.00	0.44	1.00
6.56	0	0	0.27	0.55	0	0.57	0.03	0.99	0.42	0.99
8.75	0	0	0	0	NA	1.00	0.05	0.97	0.39	0.98
overall	0.05	0	0.92	0.92	0.82	0.82	0.52	0.99	0.67	1.00

675

676 Table 4. Table showing the comparison of different estimation methods, including unconditional mean (UM, column 2),
677 median (MD, column 3), linear interpolation (LinI, column 4), logarithmic interpolation (LogI, column 5), next neighbour
678 interpolation (nNI, column 6), previous neighbour interpolation (pNI, column 7), conditional mean by regression of
679 meteorological parameters and other particle size number concentrations as inputs (CM—met and CM—PSD, column 8
680 and 9, respectively) and the feed-forward neural network with meteorological parameters and other particle size number
681 concentrations as inputs (FFNN—met and FFNN—PSD, column 10 and 11, respectively). The normalised root-mean-
682 square error (NRMSE) of each method are listed for different size bins on each row. The last row concludes the overall
683 evaluation metrics.

Particle size (µm)	Methods/ NRMSE									
	UM	MD	LinI	LogI	nNI	pNI	CM—met	CM—PSD	FFNN—met	FFNN—PSD
0.012	0.84	1.24	1.62	1.73	NA	1.62	0.74	0.23	0.69	0.11
0.015	0.92	1.26	0.45	0.42	0.79	0.55	0.72	0.30	0.59	0.03
0.021	0.91	1.24	0.21	0.22	0.46	0.61	0.70	0.02	0.58	0.01
0.027	1.04	1.28	0.24	0.22	0.46	0.25	0.77	0	0.62	0
0.037	1.08	1.34	0.15	0.15	0.27	0.35	0.85	0	0.66	0
0.049	1.09	1.43	0.13	0.12	0.46	0.46	0.95	0	0.74	0
0.066	1.04	1.50	0.23	0.18	0.66	0.49	1.04	0.01	0.83	0.01
0.088	0.84	1.42	0.16	0.13	0.65	0.61	0.96	0.02	0.71	0.02
0.12	0.59	1.25	0.22	0.16	0.86	0.80	0.74	0.03	0.54	0.02
0.15	1.59	1.13	0.66	0.53	1.64	0.96	0.58	0.10	0.49	0.05
0.21	11.6	1.61	3.7	3.24	4.93	1.53	1.26	0.85	0.71	0.31
0.37	23.8	1.42	1.35	1.12	3.12	1.06	0.70	0.22	0.54	0.07
0.49	185	14.4	4.16	3.53	7.98	1.00	0.83	0.15	0.61	0.04
0.66	672	54.5	2.42	2.32	3.62	2.79	0.82	0.17	0.56	0.03
0.88	485	39.4	2.06	2.07	2.02	2.18	2.20	1.12	1.43	0.04
1.17	1750	143	4.45	3.88	7.84	0.11	1.16	0.07	0.81	0.03
1.56	1750	143	0.19	0.22	0.11	0.46	1.16	0.05	0.81	0.03
2.08	1510	124	0.54	0.57	0.40	0.78	1.34	0.04	0.97	0.03
2.77	2880	236	0.47	0.30	1.48	0.92	1.43	0.04	1.09	0.04
3.70	5750	472	0.69	0.50	1.83	0.86	1.38	0.05	1.07	0.05
4.92	11000	902	0.51	0.34	1.64	1.02	1.32	0.09	1.00	0.07
6.56	27100	2220	1.09	0.86	2.51	0.83	1.26	0.12	0.97	0.13
8.75	52600	4320	4.95	3.33	1.62	NA	1.2	0.21	0.95	0.20
overall	1.95	2.23	0.58	0.57	0.88	0.88	1.39	0.17	1.13	0.07

Formatted: Swedish (Sweden)

Formatted: Swedish (Sweden)

Formatted: Swedish (Sweden)

Formatted: Swedish (Sweden)

Formatted: Swedish (Sweden)